A Thesis for the Degree of

Master of Engineering

Three dimensional wall motion of the carotid artery investigated by high-frequency ultrasound

Changzhu Jin

Department of Ocean System Engineering

GRADUATE SCHOOL

JEJU NATIONAL UNIVERSITY

2014. 02.

Three dimensional wall motion of the carotid artery investigated by high-frequency ultrasound

Changzhu Jin

(Supervised by Professor Dong-Guk Paeng)

A thesis submitted in partial fulfillment of the requirement
for the degree of master of engineering

2014. 02.

This thesis has been examined and approved by

Thesis director, Chong Hyun Lee, Associate Professor, Dept. of Ocean System Engineering

---

Dong-Guk Paeng, Associate Professor, Dept. of Ocean System Engineering

---

Il-Hyoung Cho, Professor, Dept. of Ocean System Engineering

2013. 12
Date

Department of Ocean System Engineering
GRADUATE SCHOOL
JEJU NATIONAL UNIVERSITY

CONTENTS

LIST OF FIGURES

ix

ABSTRACT

The characteristics of blood flow in the carotid artery bifurcation are determined by its three-dimensional geometry, which is closely related to the formation and development of atherosclerotic plaque in the carotid artery. However, the information on the cyclic changes in the vessel wall geometry of carotid artery bifurcation is limited. Present study investigated the cyclic variations of three-dimensional carotid artery geometry caused by blood flow pulsation in a rat model. A high-resolution ultrasound imaging system with a broadband scanhead centered at 40 MHz was used to obtain cross-sectional images of the rat carotid artery. The image data were acquired using an ECG gated high-frame rate mode (EKV mode) and then digitalized as an AVI video file format. Several tens of cross-sectional slices were acquired to construct three-dimensional data set. A novel automatic vessel lumen segmentation method on cross-sectional slice image was introduced in present study. The geometrical center of vessel lumen was tracked by a guide-point tracking approach which was based on correlation coefficient mapping theory. The edge of the vessel lumen was detected by a scanline edge detection method where the vessel lumen was radially scanned based on the tracked guide-point. Using the two-dimensional boundary data, the cyclic variation of three-dimensional carotid bifurcation geometry was constructed. Finally, the asymmetric three-dimensional wall motion during a cardiac cycle was investigated in both the correlation coefficient mapping approach and the automatic segmentation approach.

Chapter 1

INTRODUCTION

Stroke is one of the most common cause of death in most industrialized countries [1].Carotid atherosclerosis is a major cause of stroke and transient ischemic attack in the adult population [2]. There are many systemic risk factors that are related to the formation and development of atherosclerosis such as impaired fasting glucose, triglycerides and triglyceride-rich lipoprotein remnants, homocysteine, and high-sensitivity C-reactive protein [3]. It has been observed that the atherosclerosis occurs in specific regions of arterial tree. Nowadays it is accepted that these regions are related to local hemodynamics and wall mechanics [4-8]. Based on the studies on the relationship between hemodynamics and atherosclerosis, it is well known that the low wall shear stress (WSS) and oscillatory shear stress on arterial wall are biomarkers for the risk of atherosclerotic vascular diseases. Therefore, the study on the hemodynamics in the blood vessels can provide better understanding on the relation between blood flow and the development of the diseases such as atherosclerosis[9, 10].

A number of medical imaging systems have been developed to scan the patient's body in vivo. The imaging systems provide anatomy structure of patient or scanning object. Unfortunately, the information about WSS cannot be acquired from the current medical imaging modalities directly. Computational simulations could demonstrate the distribution

of WSS which uses the anatomy information provided by imaging modalities. The simulation is becoming considerable with the rapid evolution of computing power in recent years. The softwares, such as ANSYS (ANSYS Inc. USA), ABAQUS (Simulia, RI, USA), ADINA R&D Inc. (Watertown, MA, USA), and CONSOL (COMSOL Multiphysics, Sweden), that are based on the knowledge of finite element methods are commercially available. The initial conditions and boundary conditions as computation input parameters are extracted from medical images, and the geometry used in the simulation is image-based reconstructed geometry. However the application of this computing technique to clinical evaluation of individual patients has been limited, because it is very difficult to generate the accurate anatomical geometry in three-dimensional (3-D) [11]. The theoretical and experimental studies are performed based on simplified or idealized models which are inconsistent with real wall mechanics and hemodynamics [12-14]. Therefore, more realistic initial and boundary conditions of vessel wall motion and blood flow are necessary, and these influence the accuracy of numerical simulations.

In this study, a 3-D data set is constructed based on B-mode images acquired by a high frequency ultrasound (HFUS) imaging system from a rat model. The vessel lumen on carotid artery bifurcation (CAB) was segmented using a novel automatic lumen boundary detection and segmentation algorithm. Finally, a 3-D geometry of CAB was constructed based on the segmented 2-D lumen boundaries, and the temporal variation of the 3-D geometry has been evaluated.

1.1. Background

1.1.1. Carotid artery

1.1.1.1. Anatomy of carotid artery

Carotid arteries carry oxygen-rich blood away from the heart to the head and body. There are two carotid arteries (one on each side of the neck). The common carotid artery has two branches, the internal and external carotid arteries. The internal carotid artery supplies blood to the brain, while the external carotid artery supplies blood to other parts of the head. Turbulent and oscillatory flow occurs after the blood flow bifurcated by the geometry of the artery vessel. The vessel wall experience abnormal pressure of blood flow around bifurcation apex, where the athermatous plaques grow easily.

1.1.1.2. Carotid stenosis

Carotid artery stenosis is narrowing of the carotid arteries, usually caused by atherosclerosis. Atherosclerosis is caused by accumulation of cholesterol, fat and other substances traveling through the blood flow. These substances stick to the blood vessel walls and combine to form plaque (Fig. 1.1). Carotid artery disease is fatal because it can cause a stroke, also called a "brain attack." A stroke occurs when blood flow to brain is cut off. If blood flow is cut off for more than a few minutes, the cells in brain start to die. This damages

the parts of the body that brain cells control. A stroke can cause brain damage and; long-term disability, such as vision or speech problem, paralysis (an inability to move) or death.

It has been suggested that WSS modulates the endothelial cell phenotype and that a WSS magnitude of less than 1.5 [Pa] may lead to the degeneration of the arterial wall [15]. Under normal conditions, non-pathological tissue remodeling may occur. The combination of abnormal flow patterns and genetic predisposition could lead to formation and rupture of an atheromatous plaque. To quantify WSS, computational fluid dynamic in combination with geometrical data derived from medical imaging is needed

.
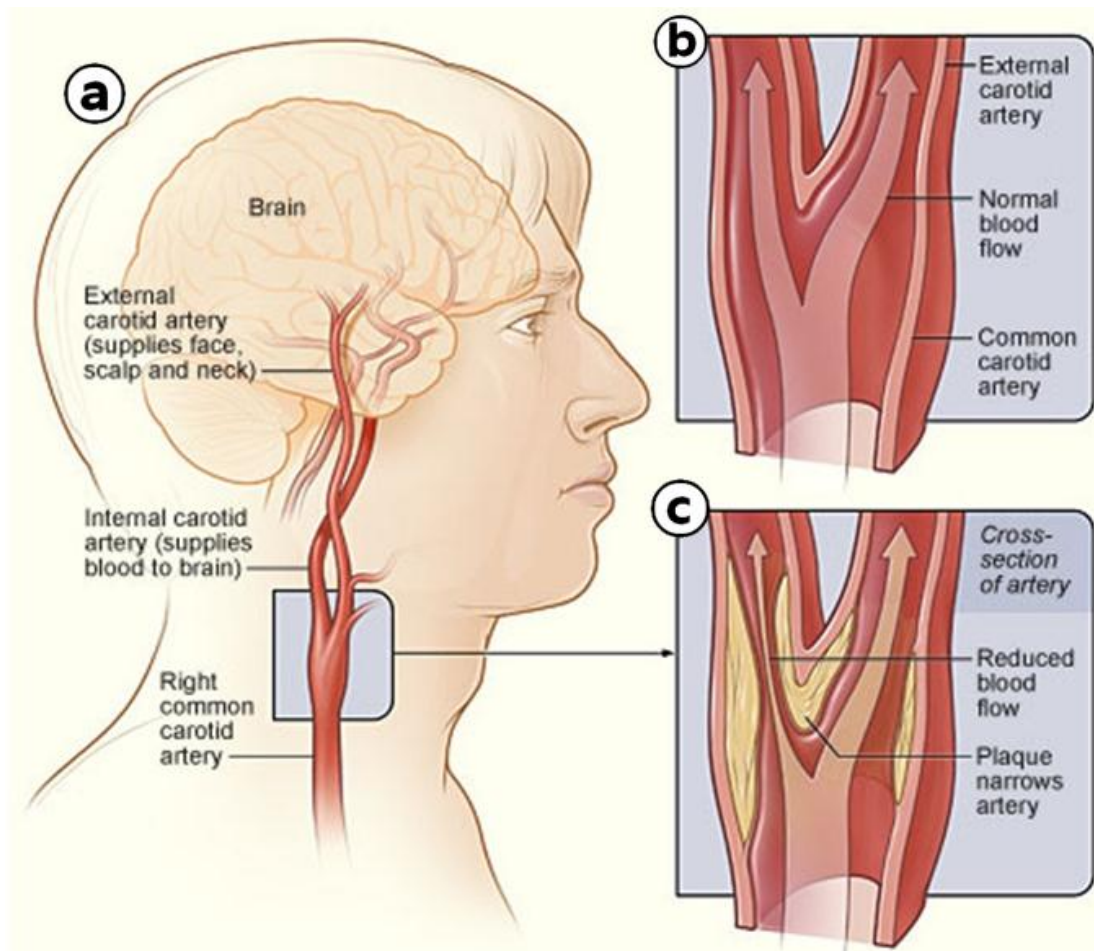
Figure 1. 1. (a) shows the location of the right carotid artery in the head and neck. (b) shows the inside of a normal carotid artery that has normal blood flow. (c) shows the inside of a carotid artery with plaque and reduced blood flow (Refer health topics in health information for the public from National Heart, Lung, and Blood Institute (NHLBI),USA.)

1.1.2. Medical ultrasound imaging and three-dimensional geometry construction

1.1.2.1. Ultrasound imaging

A significant progress is being made in the study of accurate and reproducible imaging techniques to monitor blood vessel and particular structures, namely by use of ultrasonography, intravenous digital subtraction angiography (IV-DSA), magnetic resonance imaging (MRI), and computed tomographic angiography (CTA) or 3-D-CTA. Ultrasonography imaging has several favorable properties compared with other medical imaging modalities: It does not require any injection of exogenous contrast agent that is required in radiographic computed tomography and portable ultrasonograpic imaging instruments are also available. Unlike other tomographic techniques, ultrasonography offers interactive visualization of the underlying anatomic structures in real time and has the ability to show dynamic structures within the body. The advantages of ultrasound imaging for dynamic blood or vessel motion are high temporal resolution and blood flow information by Doppler imaging. Currently the drawbacks of ultrasound imaging include a low signal to noise ratio and poor spatial resolution. Other problems with ultrasound imaging include attenuation that increases with frequency, phase aberration due to tissue inhomogeneity, and path distortion of sound propagation such as diffraction and shadowing. [16]

1.1.2.2. Rat model with high-frequency ultrasound

As the use of human subjects in medical research is limited to explorations that in no way endanger the patient's health, the need for laboratory animals is therefore obvious. Animals offer enormous possibilities to investigate different disease stages as they can be sacrificed and examined at any time point. In the present study we used a rat model, because rats are widely used and well documented as an experimental animal, and they can be easily obtained from local providers. Furthermore, noninvasive small animal imaging allows for reduction of the required numbers of animals in research by providing the possibility of long-term follow-up at various time points.

Ultrasound (US) is defined by mechanical waves with frequencies above the upper auditory limit of 20 kHz. The conventional medical US imaging devices for diagnosis commonly use frequencies ranging 3-20MHz. Because of the small size of the rat subjects and the biologic structures to be imaged, an increase in the resolution of ultrasound imaging system is in need. The commercially available high-frequency imaging systems for small animal are working in the range of 20- to 75-MHz frequency [17]. In the present study, we used an ultrasound probe with 40 MHz center frequency to scan the CAB of rat. High frame rate imaging system is also needed to construct cyclic variation of CAB. For the details about the high frame rate image acquisition are introduced in latter chapter.

1.2. Previous studies

Investigating the temporal variation of 3-D geometry on the carotid artery can improve qualitative evaluation of vessel pathology and provide quantitative data on vascular morphology and functions. A 3-D volumetric data set of the carotid artery can be constructed from multiple 2-D cross-sectional ultrasound images which are acquired by probe sweeping methods [18, 19] or by probe rotating acquisition[20, 21]. Many studies [18-21] have been done on 3-D geometry construction of carotid artery from 3-D volumetric data set. All of these researches constructed 3-D geometry of the vessel based on the manual segmentation from 2-D ultrasound images, which requires laborious and time-consuming works. The manual segmentation also requires substantial experience, and is susceptible to observer bias and variability. Jose C.R. Seabra et al. [22] have built up a semi-automatic framework based on de-speckling method for plaque segmentation and constructed 3-D geometry of vessel lumen and 3-D plaque geometry. However, the 3-D ultrasound data set was acquired from a set of images corresponding to nearly parallel cross sections through longitudinal axis of human neck manually without any kind of spatial locators. Meng Dong et al. [23] have achieved automatic detection and segmentation of bovine corpora lutea (CL) based on genetic programming and rotation invariant local binary patters. In the result of CL segmentation, some corruptions were found in the segmented binary edge images, which meant missing information in constructing artery anatomy. More realistic data acquisition with less boundary corruption of edge detection is needed for 3-D geometry reconstruction

work. While automatic and semi-automatic approach would be easier to use, it must be validated to ensure that the results agree with manual segmentation by a trained operator. The segmentation performed by an operator is normally reliable the most, and is usually considered as the surrogate gold standard used to validate reliability of semi-automatic segmentation methods [24-26].

Although many researches have provided acceptable results on 3-D geometry reconstruction using ultrasound images acquired from patients, each method and approach highly depends on the quality of the 2D images. In small animal experiment, the ultrasound image was measured using high frequency ultrasound images. The algorithms suggested in previous study [27] were processed using closed or almost-closed vessel lumen ultrasound images, which applied a threshold method and Hough-Transform to detect the edge boundary appropriately. In high frequency ultrasound images, the shadow artifacts and low contrast resolution of ultrasound image shows un-closed lumen boundary. Therefore, a robust edge detection method with reliable 3-D data acquisition is required.

The accurate numerical models are important and useful tools to understand atherosclerotic plaque growing-up, progression, vulnerability as rupture in human vessels. As mentioned in previous chapter these numerical models can be used to evaluate WSS, to compute wall stresses and to correlated blood flow and geometrical feature with atherosclerotic pathologies. The numerical simulation considering cyclic variation of vessel wall geometry which in present study could provide more accurate and realistic WSS

distribution.

1.3. Specific Aims

The objective of the present research is to reconstruct 3-D geometry of carotid artery during vascular cyclic variation. To accomplish this objective, the aims of this research are subdivided into three as follows.

The first aim is to acquire serial cross-sectional B-mode images from a rat subject. The serial image acquisition has been performed using a commercially available small animal imaging system, Vevo 770 (VisualSonics Inc., Toronto, ON, Canada).

The second aim is to build up a segmentation method which can segment the vessel lumen boundary. A novel boundary detection method combining correlation coefficient mapping with a scanline edge detection has been introduced for vessel lumen segmentation.

The last aim is to construct 3-D geometry from segmented two dimensional slice images. The cyclic variation of 3-D geometry and asymmetric variation have been evaluated.

The cyclic variation of 3-D vascular geometry could provide useful information for the numerical simulation.

1.4. Thesis Outline

Chapter 2 provides the materials and imaging system. The description starts with ultrasound imaging acquisition system setup and the details about a rat model. The special mode (EKV mode) of image acquisition is introduced and the evaluation of acquired images is presented latter.

Chapter 3 presents the image processing procedures. This chapter presents segmentation of 2-D lumen boundary of vessel lumen by CCM guide point tracking approach and scanline edge detection approach.

Chapter 4 shows constructed 3-D geometry by three different methods, manual segmentation, cross correlation mapping method, and a suggested novel technique. The results show the cyclic variation of carotid artery bifurcation geometry.

Chapter 5 discusses the segmentation methods and the results of the constructed 3-D geometry. This is the first automatic segmentation using a correlation coefficient mapping approach combined with scanline edge detection.

Chapter 6 concludes the results of this study and suggests future directions for research.

Chapter 2

MATERIALS AND ULTRASOUND IMAGING SYSTEM

2.1. Rat experiments

A Spargue-Dawley rat (8 weeks old) was anesthetized with isoflurane and oxygen via a vaporizer and placed in a supine pose on a heated stage. A physiological monitoring unit (THM 100, Indus Instruments, Houston, TX, USA) was installed to monitor rectal temperature, heart rate, and electrocardiogram (ECG). The neck fur on the left side was gently removed using thioglycolate depilatory cream (Veet, Reckith Benckiser Inc., Toronto, ON, Canada) and pre-warmed ultrasound gel was used as an acoustic coupling medium. All procedures performed on animals were approved by the Animal Care and Use Committee of Jeju National University (Jeju, South Korea) to ensure that they were appropriate and humane.

2.2. Image acquisition

The rat left common carotid arterial images were collected by a Vevo 770 ultrasound imaging system (VisualSonics Inc., Toronto, ON, Canada) using a single-element crystal mechanical transducer (RMV 704; VisualSonics Inc., Toronto, ON, Canada). The axial and lateral resolutions are $40\,\mu m$ and $80\,\mu m$, respectively. The focal length of the scanhead is $6\,mm$ and depth of field (DOF) is about $1.5\,mm$. A $4 \times 4\,mm$ field of view was set to

obtain the cross-sectional carotid artery images. The scanhead was mounted in a xyz positioner of an integrated rail system which allowed precise image acquisition from a variety of positions and angles. After adjusting the scanhead using B-mode window, the high-temporal resolution cross-sectional images were acquired by switching to ECG-gated kilohertz visualization (EKV) mode. The data were saved as AVI video file format for further analysis.

Probe: RMV 704 (40 MHz)

Animal stage: ECG (①), XYZ positioner (②), Anesthesia system
Temperature controller (③).   : isoflurane inhalation
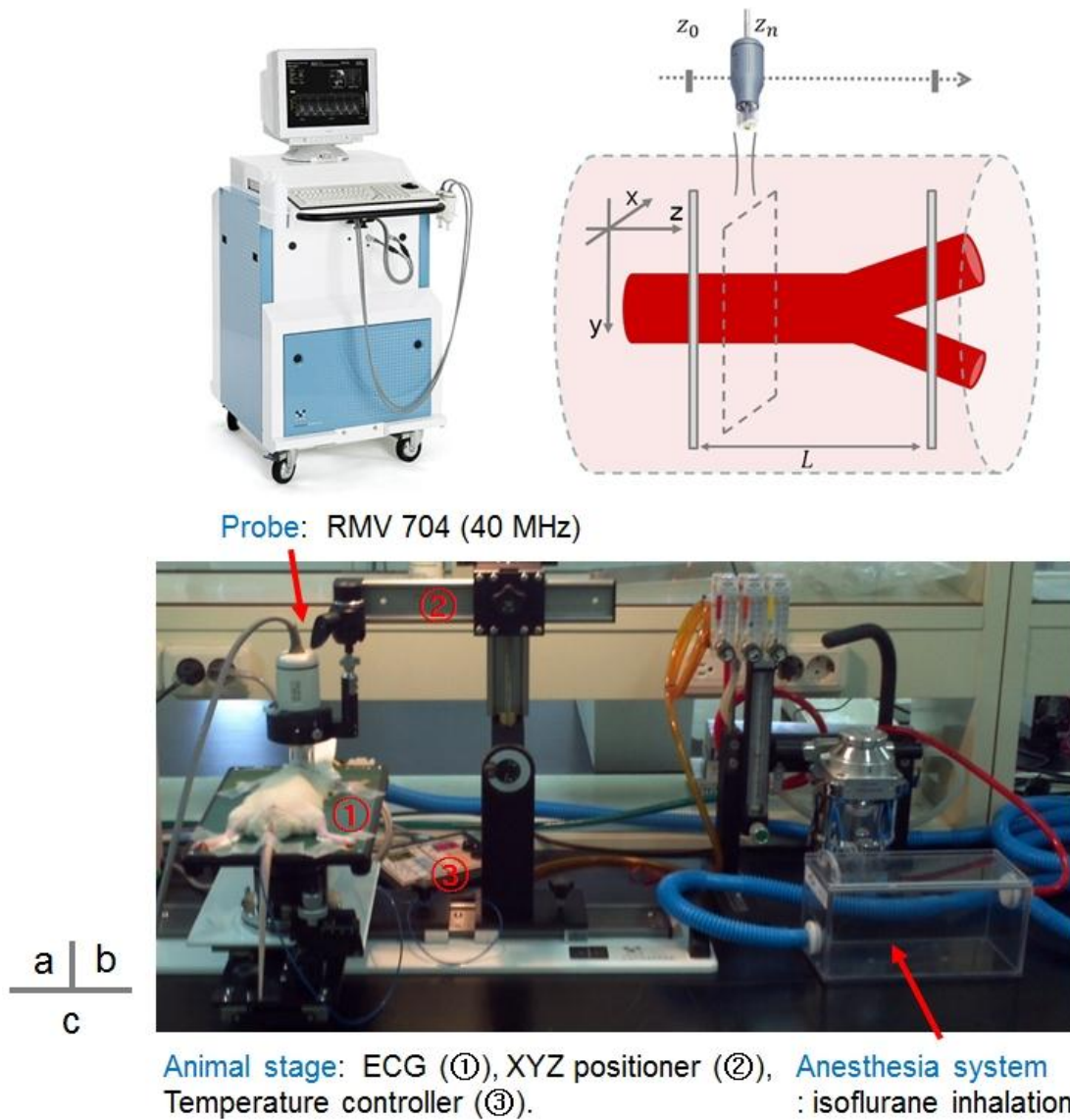
Figure 2. 1. System setup for ultrasound imaging. (a) shows the Vevo 770 ultrasound imaging system. (b) shows the image acquisition protocol. The images were acquired by sweeping the scanhead linearly along z coordinate from scan point z_0 to z_n. We measured 31 slice images for analysis. (c) shows the rat model setting stage.

2.2.1. EKV mode

High frequency ultrasound images were obtained using a single element mechanical sector scan probe. Typical frame rates of ultrasound B-mode (UBM) range from 30 to 60 frames per second, depending on the scan width, the scan depth, and the transducer beam width [17]. Considering these frame rates and heart beating rate of an adult rat (around 300 beats per minute), the traditional B-mode imaging that just provides tens of frame images per cardiac cycle is not enough to precisely examine the cyclic variation of arterial movement of rats.

EKV mode image acquisition overcomes this limitation because it provides a high frame rate cine loop with 1000 frame rates per second. In the EKV mode, the transducer works on a line-by-line basis like multiple M-modes. The transducer transmits a pulse ultrasound signal and receives ultrasound echoes at the same position to collect data during a cycle. After data acquisition at previous position, the system moves the transducer to next position, and then repeats the transmission and acquisition. Several minutes are required to collect required RF signals. At the end, the acquired RF signals are sorted and averaged synchronized with ECG signal, and are reconstructed into an EKV cine loop of one cardiac cycle at high-temporal resolution of 1000 frames per second [17].
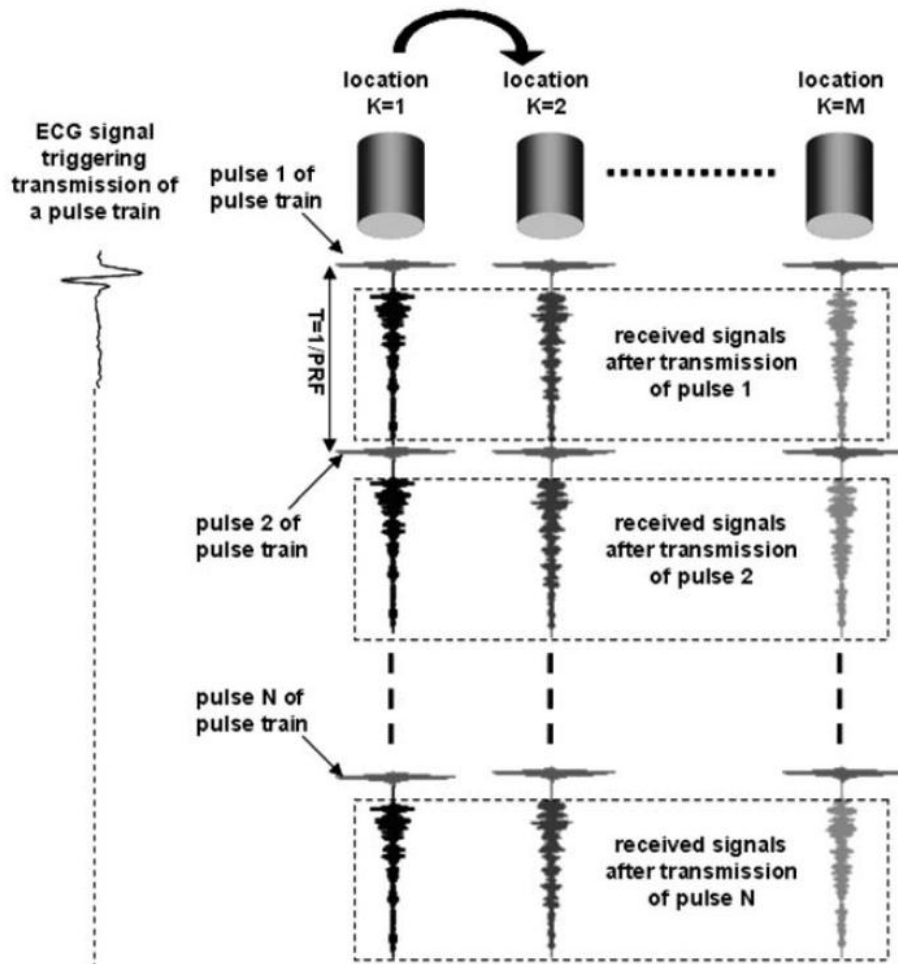
Figure 2. 2. The principle of EKV data acquisition. The transducer is kept fixed relative to the tissue during transmission of the pulse train and the acquisition of the subsequent backscattered signals. [17]

2.2.2. Acquired image evaluation

The low contrast boundary with shadow artifact remains as a challenge for the edge detection. The traditional global-threshold edge detection failed in this non-closed vessel lumen boundary case. Because of the open-like lumen boundary the gray-scale value is relatively lower than the closed area. In this case the threshold approach provides over or less segmented results. The Hough transform approach [27] also provides low trustworthy detection in these US images. Ying Li et al. [28] applied Hough transform to fit the binary edge images after threshold process. At the result, the detected lumen center was shifted to left side of the actual lumen center, which was not appropriate to edge detection for 3-D geometry construction. However, the purpose of their work was to evaluate the echo variance in the central area of the lumen, so accurate edge detection was not necessary. Nevertheless, they provided reasonable results on the relationship between smoking effects and echogenicity of carotid artery. Figure 2.3 shows the measured US image in the present study.
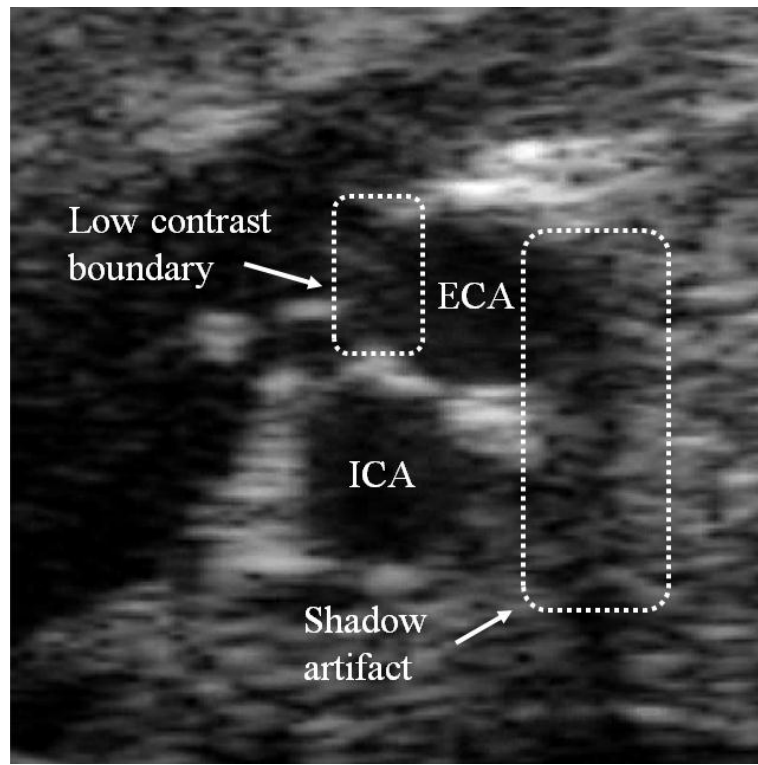
Figure 2. 3. The frame image at the downstream of the bifurcation apex. The upper black circle shape is external carotid artery (ECA) lumen and the lower black circle shape is internal carotid artery (ECA). The dash-line block at the right side shows shadow artifact and the left side dash-line block shows low contrast un-closed boundary.

Chapter 3

IMAGE PROCESSING

3.1. Manually vessel lumen segmentation

J.Renner et al. [29] selected 10 points manually at each slice image in the lumen boundary. The entire lumen surface was formed by approximately 1000 points to describe a 3-D anatomy. Egger et al. [26] proposed another manual segmentation method. The expert first identified and confirmed the location of the bifurcation, and defined an approximate medial axis of the carotid artery by choosing two end points of the axis. The multiplanar 3-D viewing software presented 2-D images of the artery by slicing through the 3-D image orthogonally to the medial axis. Then the expert contoured the lumen boundaries on each of these images.

The manual segmentation in this study was performed by using a commercial image processing software (ScanIP) which provided a painting tool with other standard image processing toolkits. First, a standard point (SP) was selected on the distinct lumen edge which usually set on the brightest gray level pixel on the lumen boundary. Then, using large circular brush, the entire lumen area was painted based on the SP. These slice images ($slice\ number = 31$) were painted by an operator, and then these images rendered to 3-D using the image processing software. Figure 2.4 shows the procedure of the manual segmentation.
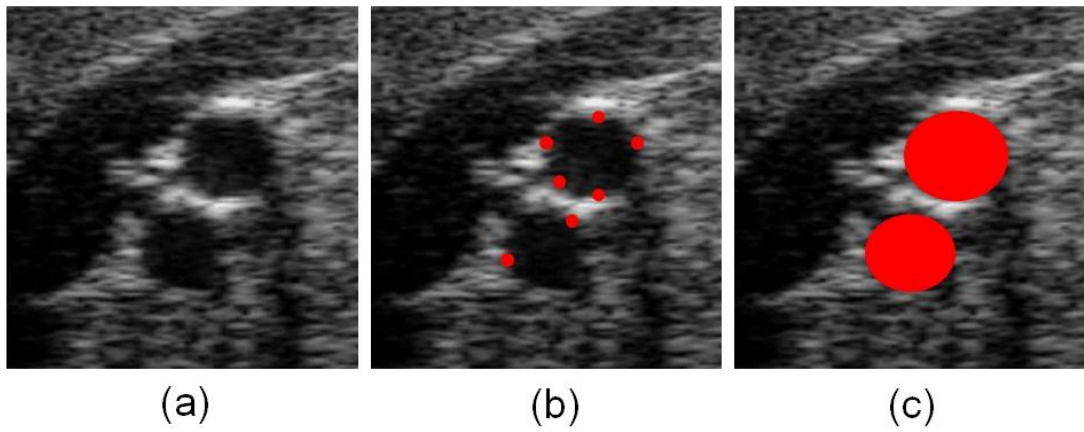
Figure 3. 1. (a) is a gray-scale image cropped from the 12th slice image in EKV data and (b) shows standard guide points which were manually selected. (c) shows the painted lumen area based on the standard guide points.

3.2. Automatic vessel lumen segmentation

According to the image quality and the operating system, there can be different approaches for the vessel lumen boundary segmentation. In particular, for the US images with low contrast and shadow artifacts, we introduced a novel automatic segmentation method to overcome the drawbacks in low image quality.

3.2.1. Correlation coefficient mapping (CCM)

The first step of the image processing is to define the region of interested (ROI). A rectangular ROI window of $(900 \times 800)\ pixel$ was cropped from an EKV frame image to reduce the computation load in the following processes. Then the ROI window divided into several small sub-blocks in size of $(l \times l)\ pixel$ to calculate the correlation coefficient (CC). The size of the sub-block can be set arbitrary, and different size of sub-block provides different resolution of CCM as show in Figure 2.6. In this study we set the size of block as $(12 \times 12)\ pxiel$. The 2-D CC was simply calculated by using the following equation.

$$V_{cc} = \frac{\sum_{i,j}\left(SB_{mn}^{fn}(i,j) - \overline{SB_{mn}^{fn}}\right)\left(SB_{mn}^{fn+1}(i,j) - \overline{SB_{mn}^{fn+1}}\right)}{\sqrt{\left(\sum_{i,j}\left(SB_{mn}^{fn}(i,j) - \overline{SB_{mn}^{fn}}\right)^2\right)\left(\sum_{i,j}\left(SB_{mn}^{fn+1}(i,j) - \overline{SB_{mn}^{fn+1}}\right)^2\right)}}$$

Where V_{cc} is the value of CC between two sub-blocks $SB_{mn}^{fn}(i,j)$ and $SB_{mn}^{fn+1}(i,j)$. The first sub-block was cropped from the frame number of fn, and the second one was cropped

from next frame. (m, n) is the location of the sub-block in ROI image, $\overline{SB_{mn}^{fn}}$ and $\overline{SB_{mn}^{fn+1}}$ are the mean of the gray scale value of sub-block $SB_{mn}^{fn}(i, j)$ and $SB_{mn}^{fn+1}(i, j)$, respectively.

After calculation of 2-D CC between two temporal sub-blocks, the CC was saved as color scale value in pixel location of (m, n) in another new image which is CCM. Figure 2.7 shows overall calculation procedure of CCM. After calculating the CC of sub-blocks in location of (m, n), shifting the sub-block to next neighbor pixel like $(m + 1, n)$ or $(m, n + 1)$. After iteratively calculating the CC between all sub-blocks, the correlation map was obtained at the end.

Note that the size of CCM image was shrinking down after primary calculation and CC positioning. The total loosing pixel number from ROI window to CCM is $IS_{ROI} - \left(\left(S_c - (l - 1) \right) \times \left(S_r - (l - 1) \right) \right)$. There needs resizing procedure for changing CCM image size as the same as ROI window. Here IS_{ROI} is the image size of ROI window, S_c is size of the column and S_r is size of row in the ROI window.
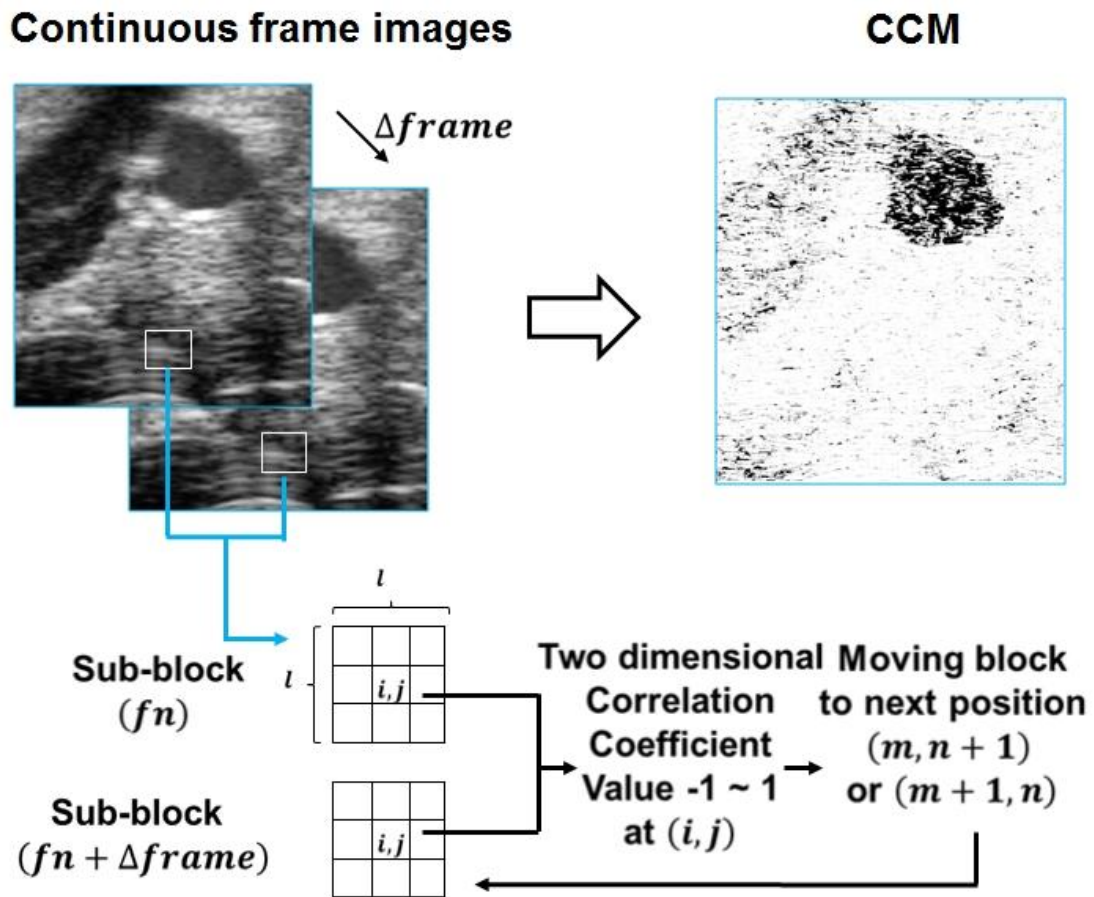
Figure 3. 2. The work flow of cross correlation (CC) calculation. Two-dimensional correlation coefficient was calculated on the selected sub-block in the position of (m, n) from two continuous frame images. Storing the CC value on the pixel position (m, n) in new image and shift sub-block to next position and repeat CC calculation and storing work until the sub-block is traveled all over the region of interest (ROI) image.
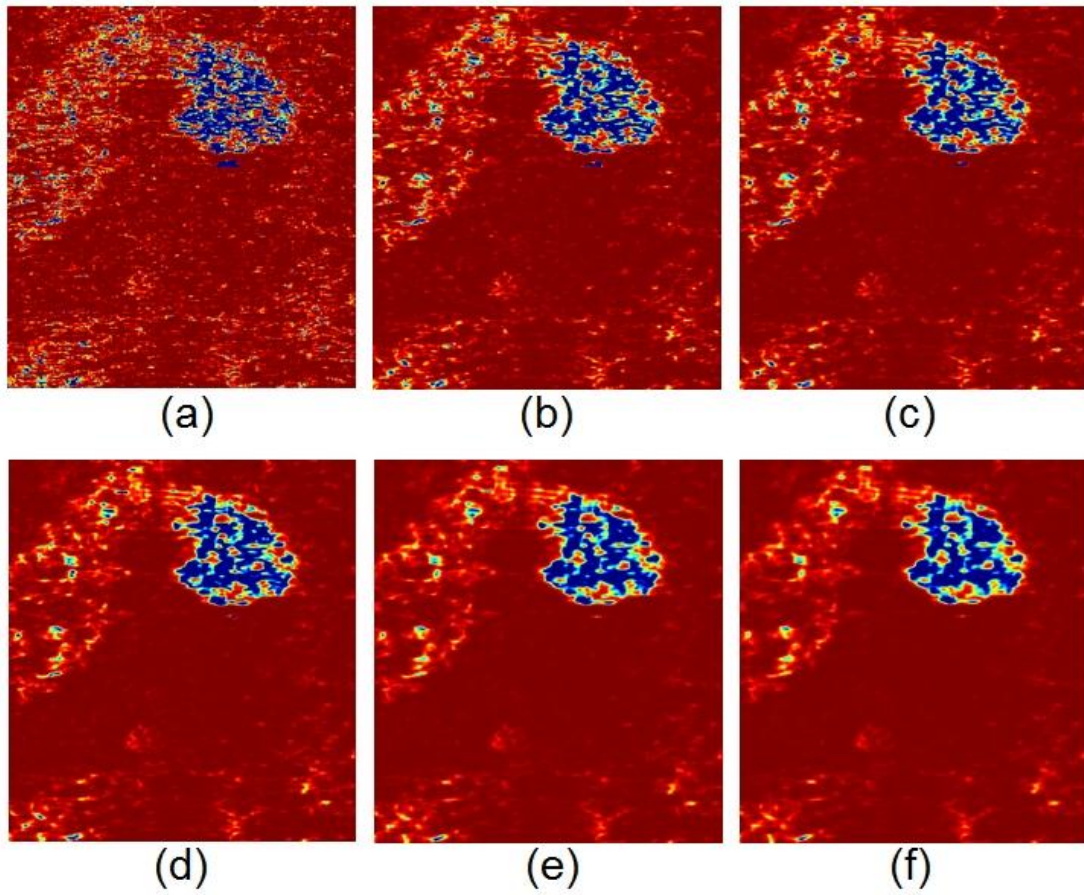
Figure 3. 3. The color maps of the cross correlation map (CCM) images calculated by different sub-block size. The sub-block size are (3×3), (10×10), (12×12), (15×15), (18×18), and (20×20) pixel respectively.

Gray scale image   **CCM image**

(a)   (b)
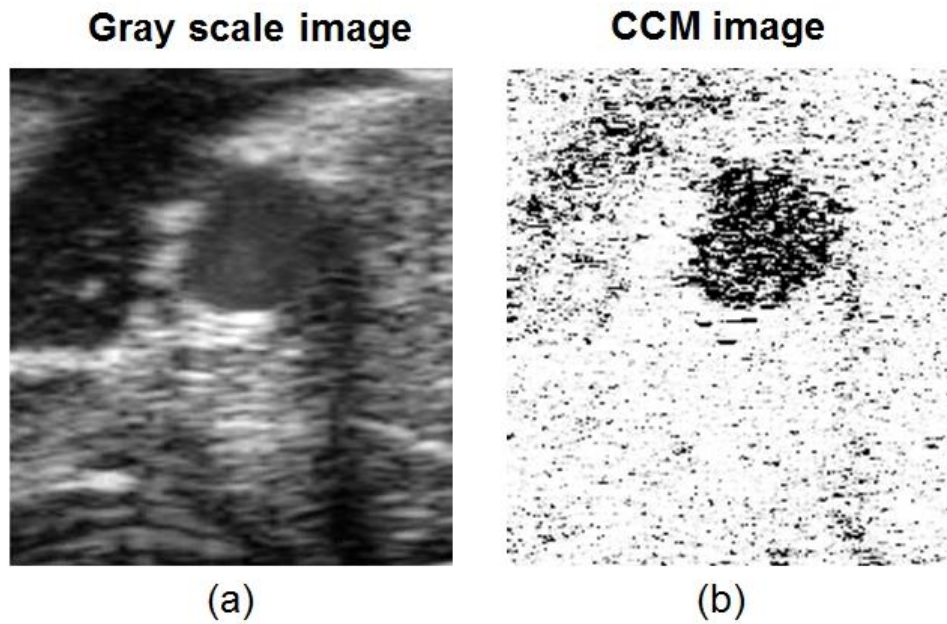
Figure 3. 4. (a) is the gray-scale image cropped from EKV data and (b) is the CCM image calculated using frame fn and fn + 1 images. The brighter part means lower correlation coefficient. From these two images we can easily see that the shadow artifact was nearly removed and the low contrast boundary was improved.

3.2.2. Guide point tracking from CCM

Figure 3.5 shows the procedure of an automatic guide point tracking method. The process has divided to three parts.

The first part is prior image processes that combine 4 steps. The sub-results in each step show on the top right corner of Figure 3.5. The global threshold converts gray-scale CCM image to binary one. The binary image of the CCM includes the large borders, and then there need an additional process to clean the rest of the large border.

The second part during tracking procedure is the case classification. The cleaned boundary was classified into three cases. The first case combines one closed boundary with one guide point where the slice location is closed to CCA. The second case combines one closed boundary with two guide points. The slice location of this case is closed to bifurcation starting area (bifurcation apex). The third case combines two closed boundaries with two guide points which were located in downstream of the apex. If there is one closed boundary after border cleaning, the classifying system will check the shape of the boundary. The circle shaped boundary will be classified as case one and the ellipse shaped boundary will be classified as case two.

The third part shows classification results in three cases. The guide points were located in the center of the selected boundary. These points would be used as guide point on scanline edge detection in later process.

During guide point tracking procedure, a global threshold was used for thresholding the

gray-scale image to binary image. Even the binary image highly depends on the threshold value, the guide point still occurs inside of the selected closed-boundary. The center points which will be used in Scanline edge detection are not necessary to exactly locate the geometry center of the vessel lumen. So the location variation of guide point during the thresholding in different frame images is not critical for the use as a center point in further process.
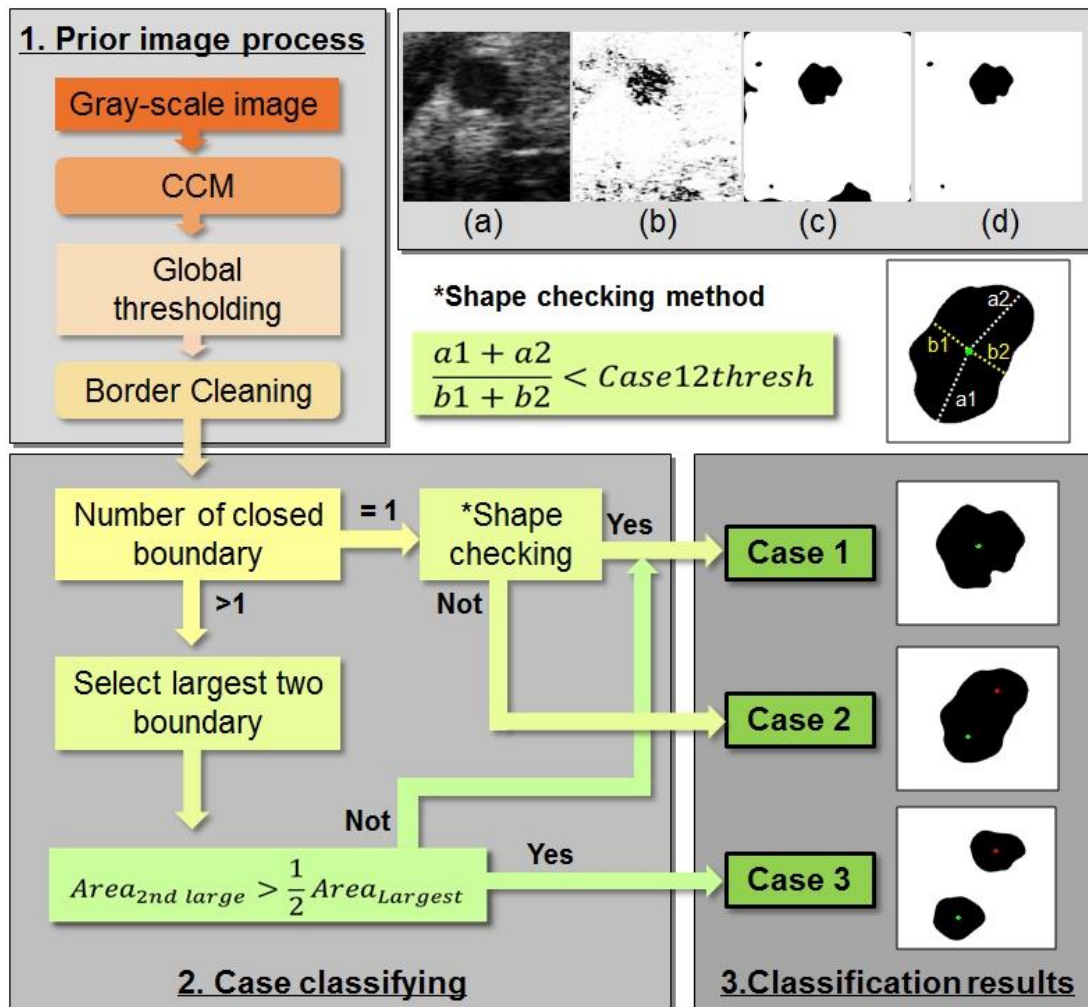
Figure 3. 5. The automatic guide point detection procedure. There have three steps for guide point detection. A large closed-boundary remained binary image was provided after prior image process. (a) is gray scale image and (b) is calculated CCM image. (c) is binary image after took global threshold on CCM and (d) shows remained boundary after cleaning the large borders. The binary images classified to three cases during classifying process and guide points have tracked. Especially when classifying case 1 and case 2, a shape checking method was used. The letter $a1$ and $a2$ means the largest distances from guide point to edges, and $b1$ and $b2$ means the shortest distances from guide point to edges.

3.2.3. Scanline algorithm

The edge detection in this study has used a scanline algorithm to scan the vessel lumen radially based on the guide point which was tracked in previous process. As Figure 3.6 shows, the Scanline is defined as $R_k^{fn}(\theta)$ which contains three variables. The letter θ denotes the scan angle of the scan line; it provides the location information of the Scanline in polar coordinate. The letter fn represents the frame number of the processing image, and k presents slice number which denotes the spatial location of the processing images. The number of the scanline is defined by the sweeping angle $\Delta\theta$ and the following formula explains the relationship. The relation between rectangular coordinate and polar coordinate is also explained in following formulas.

$$number\ of\ Scanline = \frac{2\pi}{\Delta\theta}$$

$$R_k^{fn}(\theta) = P_k^{fn}(i,j)$$

$$i = R_k^{fn}(\theta) \times cos\theta, j = R_k^{fn}(\theta) \times sin\theta$$

The basic principle of the Scanline approach is to detect the edges on one dimensional gray-scale value on each Scanline. Before scanning the vessel lumen, several variables are needed to be defined. They are starting-ending length of the Scanline and sweeping angle. The scanline length limitation reduces the size of calculating data and computation time.

The US image pixel is usually stored in the rectangular coordinate like $P_k^{fn}(i,j)$ but the scanline was in polar coordinate. In order to obtain the 1-D gray-scale values of scanline, it is needed to find the scanline matched gray-scale values in the rectangular coordinate as

shown in Figure 3.6 (a). The relationship between polar coordinate and rectangular coordinate is described in previous equations. As shown in Figure 3.6 (b), during this process, the system stores each related gray-scale value of scanline pixels as 1-D gray scale value. These scanline data will be used in edge detection process as shown in Figure 3.6 (c).

The edge detection in scanline method used a simple approach. The first step is to define an interpolated line based on this gray-scale value, which is plotted in Figure 3.6 (c). The raw gray-scale value with interpolation provides a smoothing curve. During interpolation, the shape of raw data has been changed but the variation trend was not significantly changed. Then the peak point on the interpolated line was found. The peak point is an important criterion when finding the edge position. The peak point is a maximum value of turning points that are plotted in Figure 3.6 (c) as small red circles. There is one exception, when there is no turning point on the interpolated curve.. In this particular case, we define the peak point located at a proportional position between mean value line and the maximum value point of the interpolated curve. The peak point plotted in Figure 3.6 (c) as a small broad-circle. An edge point has been defined based on the relation among mean value line, peak point and the intersection points. The intersection points are intersected points between mean value line and the interpolated curve. The intersection point which is located at the left side of the peak point was defined as an edge point. The edge point is plotted in Figure 3.6 (c) as small rectangular. Figure 3.6 (d) shows the primary detected result and the fitted edge.

As Figure 3.6 shows the primary detected edge are located in different length of radius from guide point. The secondary fitted edge which using polynomial fitting is well bounding the vessel lumen. Using this approach the lumen boundary is segmented in each slice image including bifurcation and downstream of apex.
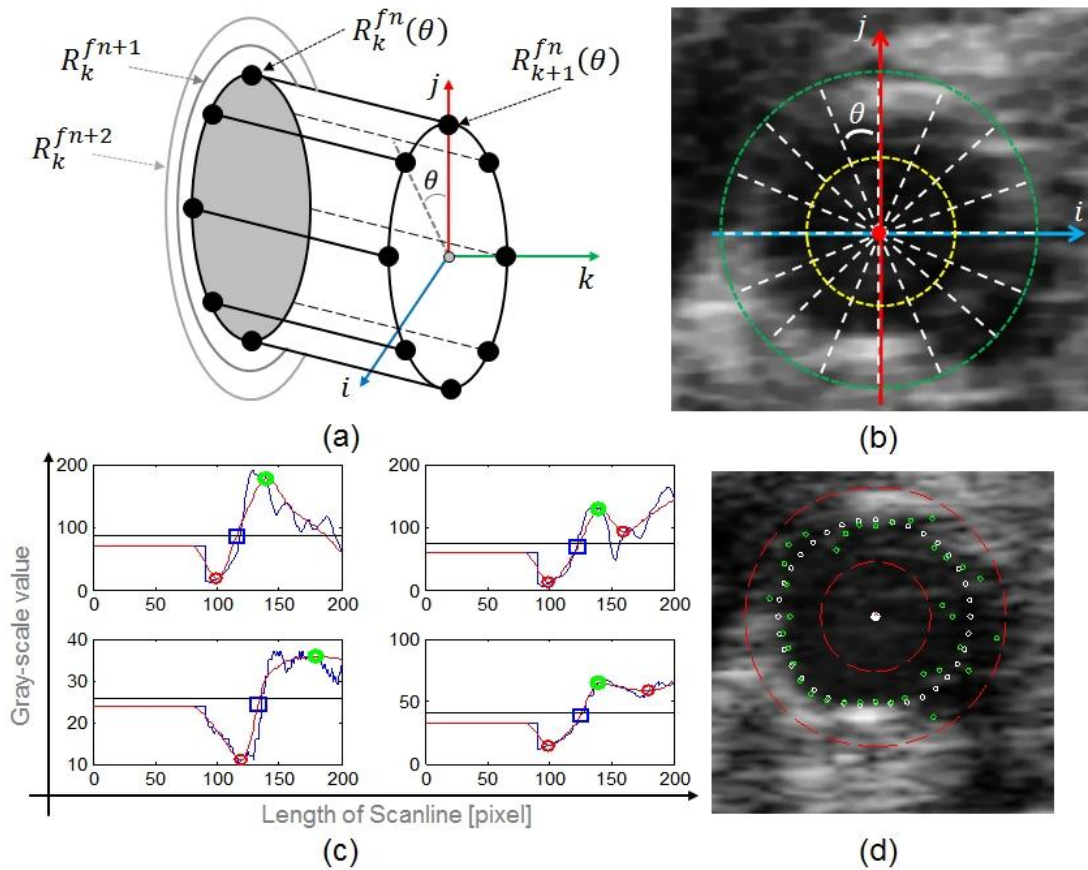
Figure 3.6. (a) shows sketch of the coordinate system used in Scanline algorithm. Where letter θ is sweeping angle and k denotes the spatial position of the slice image. (b) shows the cross-sectional gray-scale image and the white dash line denotes the Scanline. The yellow dash line is starting line of the Scanline and the green dash line is ending line of the Scanline. (c) shows the edge detection process. The small green circle denotes the peak point and the small red circle means the turning points. The small blue block is the edge we want to define. (d) shows the detected result.

Chapter 4

THREE DIMEONSIONAL GEOMETRY

4.1 Automatic boundary segmentation

As shown in Figure 4.1 b) and d), the automatic edge segmentation was achieved to be in agreement with CCA. Comparing these with the segmented result provided by Li Ying et al. [28], we can find that the one side shifted segmentation observed in Hough transform was almost disappeared..

The automatic segmentation method provided in this study can be used in lumen boundary detection in CCA. Even for low contrast images, the segmentation approach provides quit robust results.
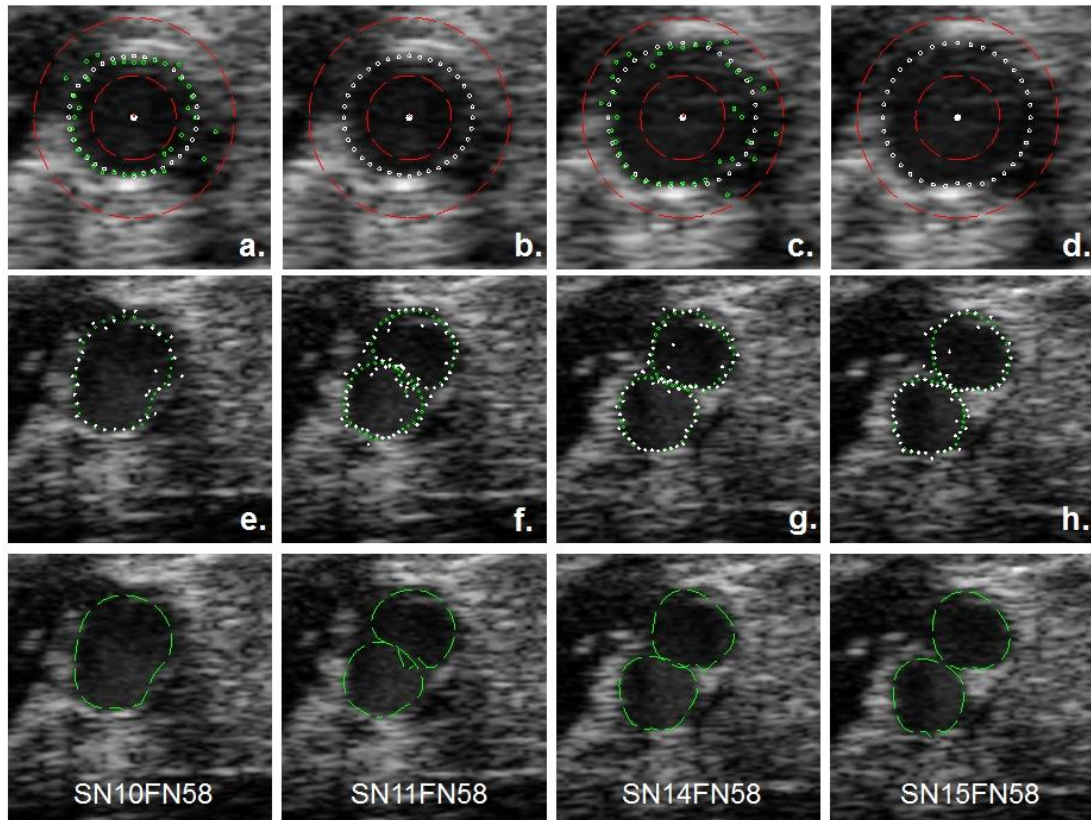
Figure 4. 1. The green dotted circle presents the result of automatic segmented edge at systole and the white dotted circle means fitted edge. The segmented boundary was plotted alone in (b). (c) and (d) show the segmented results in diastolic phase. (e)~ (h) show the segmented results in different slices at the same cyclic phase (diastole). The green dash line presents the segmented boundary.

4.2 Three-dimensional geometry construction procedure

The 3-D geometry construction was achieved in commercial image processing software ScanIP (Simpleware Inc., UK). The process is described in detail in Figure 4.2. Note that the 3-D geometry shown in Figure 4.2 (f) is based on the CCM images; the geometry does not present the 3-D geometry of the actual vessel lumen.

It will be failed if this process is applied on gray-scale image, because the lumen boundary in gray-scale image is not as clear as that in CCM image. Applying a global threshold on the gray-scale image, the boundary in the resultant binary image carries many erosion and bulge area.

The manually segmented boundary in previous study was time consuming process. We overcame this drawback with an automatic segmentation method based on Scanline edge detection. The 3-D geometry construction works based on manual segmented image and automatic segmented image used this image processing software. In these two cases we skipped the processes of a), b), c) and d) as shown in Figure 4.2.
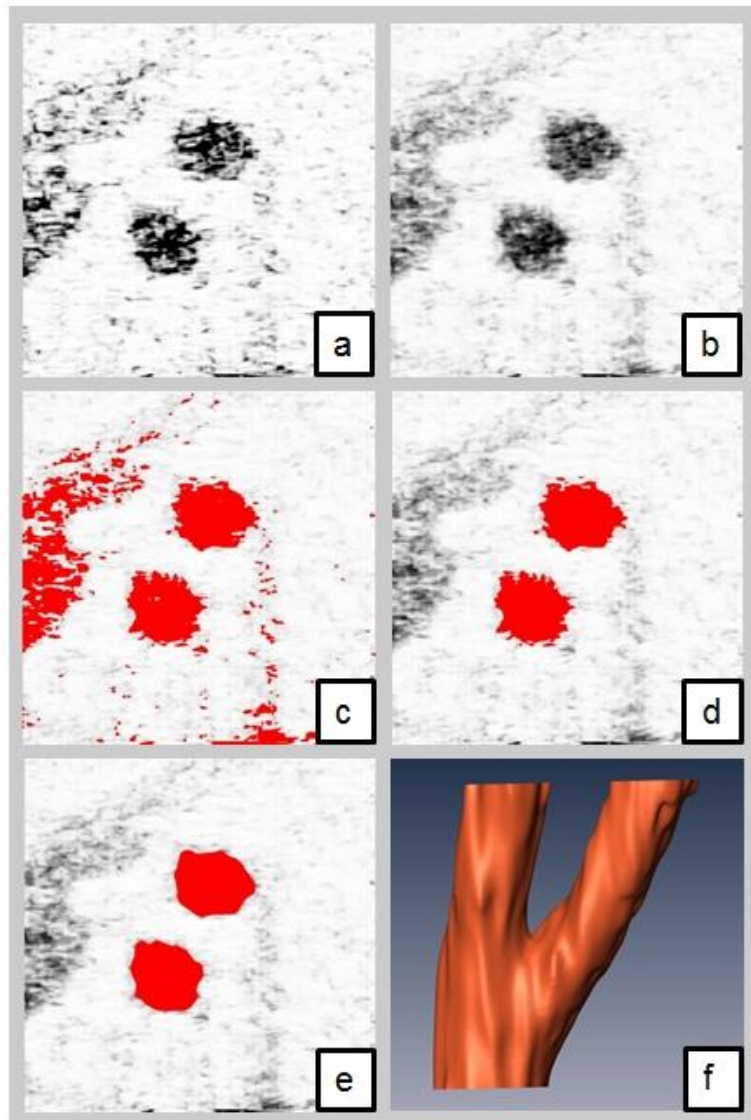
Figure 4. 2. The 3-D geometry construction procedure using manual boundary segmentation. (a) and (b) shows the intact and mean filtered CCM images, respectively. The segmented boundaries after thresholding and cleaning islands are shown in (c) and (d). The smoothed boundary using median filtering is shown in (e). The final 3-D geometry constructed from 2-D segmented slice images is shown in (f).

4.3. Three-dimensional geometry on three different cases

3-D geometry based on CCM slice images, automatic segmented images and manually segmented images were presented in this section. Figure 4.3 shows the constructed 3-D geometry in three cases. From Figure b) and c) we know the shape of two cases is not much different. The ICA on both manual and automatic segmentation cases shows smooth surfaces, but the automatic segmentation case shows relatively rough surfaces on ECA.

Figure 4.4 shows temporal variation of 3-D geometry based on CCM slice images and automatic segmented images. Both of these cases were constructed on the images of frame number 2, 8, 14, 20, 38, 44, 50 and 58. In this study of the 3-D geometries we have constructed only the expansion phases of the carotid artery. The frame No. 2 and frame No. 58 present systole and diastole of vascular phase respectively.
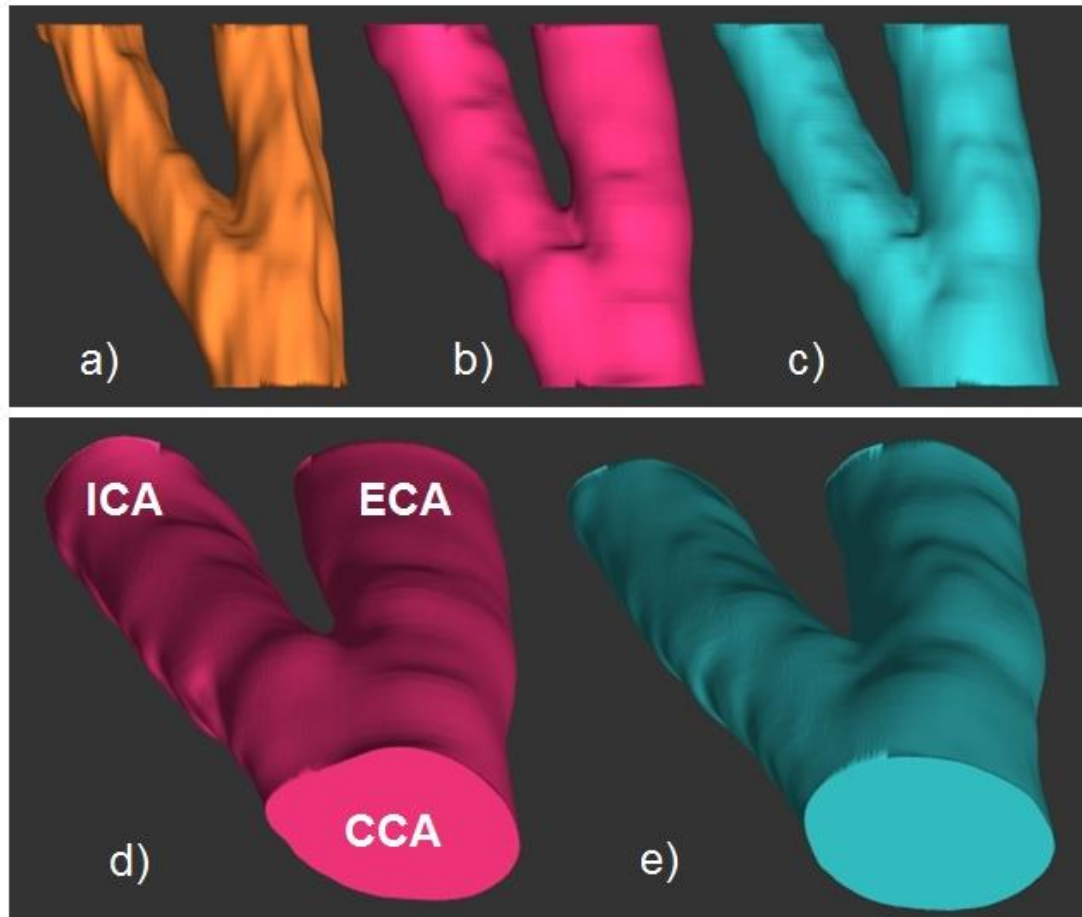
Figure 4. 3. The 3-D geometry construction results on frame number 20. (a) is constructed geometry based on CCM images, (b) shows the geometry based on automatic segmentation, (c) presents the geometry based on manual segmentation. (d) and (e) show the upward view of geometry based on automatic segmentation and based on manual segmentation based on manual segmentation respectively.
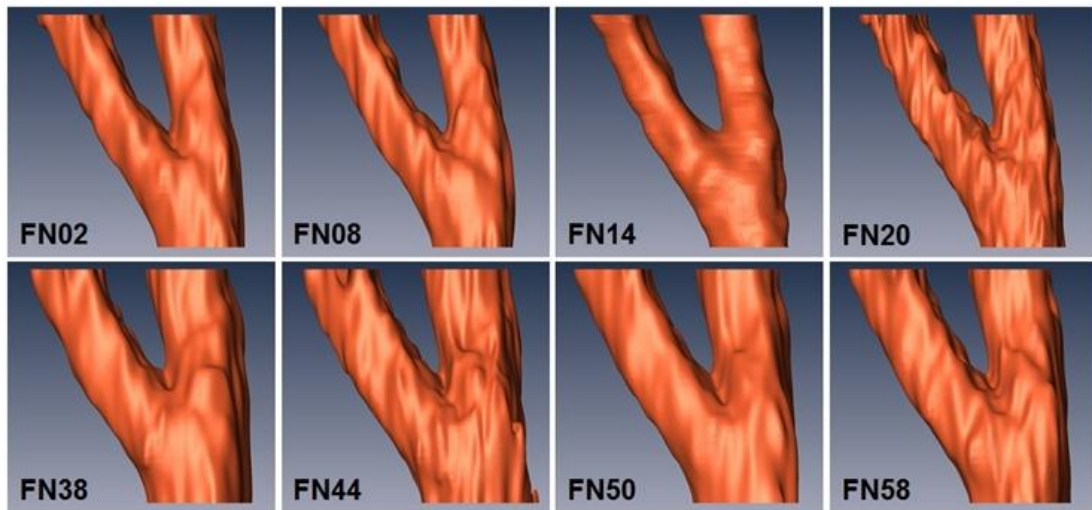
Temporal variation of 3-D geometry based on CCM slice images
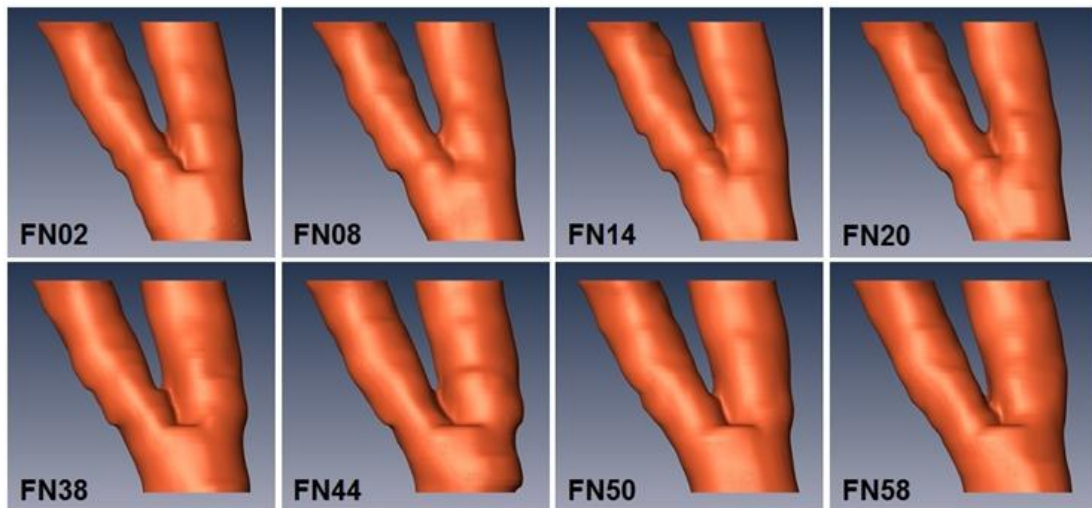
Temporal variation of 3-D geometry based on automatic segmentation

Figure 4. 4. The temporal variation of 3-D geometry based on CCM images and automatic segmentation. The frame No. 2 and frame No.3 presents 3-D geometry on the phase of systole and diastole during a vascular cycle.

4.4. Three-dimensional geometry on systolic and diastolic phase

The three dimensional geometry on systolic and diastolic phases was presented in this section. A significant difference in wall displacement amplitude between the anterior and posterior wall was observed during a vascular cycle. The constructed 3-D geometry based on CCM slice images and automatic segmentation was plotted in Figure 4.5 and Figure 4.6. In this section the manually segmented case was not considered.

The asymmetry of radial wall motion was noticeable in the downstream region near the bifurcation. As the results of 2-D analysis on carotid artery bifurcation by Nam et al. [2], the results of 3-D also indicate the geometrical variation of the carotid artery lumen at systole and diastole.

The 3-D geometry based on CCM slice image does not present the actual vessel lumen, but the wall motion during a vascular cyclic is similar to the automatic segmentation 3-D geometry. The present results of CCM based geometry and automatic segmentation based geometry demonstrate that the carotid bifurcation of rats expands preferentially to the anterior direction.
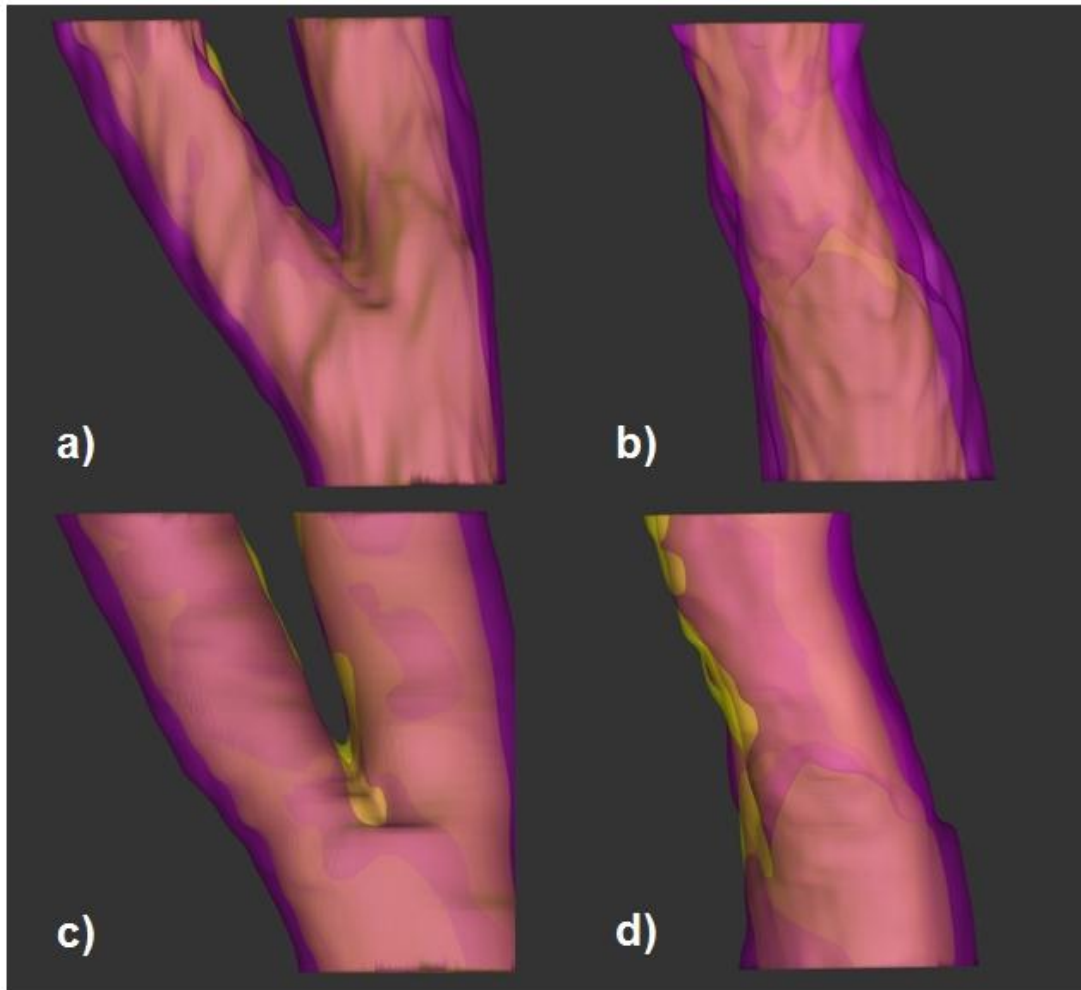
Figure 4. 5. (a) and (c) show front views of systolic and diastolic 3-D geometry based on CCM slice images and automatic segmentation respectively. (b) and (d) show the side views of the geometries.
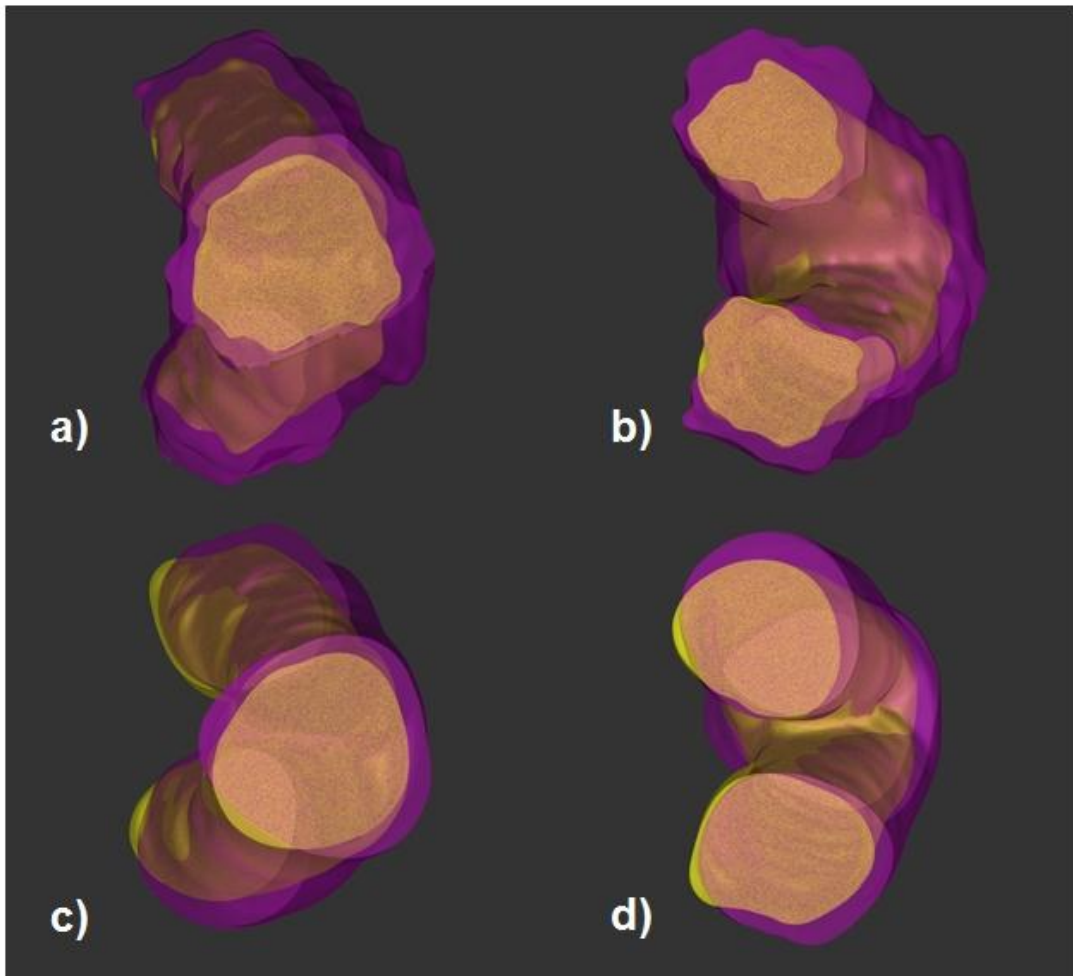
Figure 4. 6. (a) and (c) show upward views of the systolic and diastolic 3-D geometry based on CCM slice images and automatic segmentation respectively. (b) and (d) show the top views of the geometries.

Chapter 5

PRELIMINARY STUDY ON NUMERICAL SIMULATION

5.1. Previous study on numerical simulation

The accurate numerical models are important and useful tools to understand atherosclerotic plaque formation, progression, vulnerability for rupture in human vessels. As mentioned in previous chapter these numerical models can be used to evaluate WSS, to compute wall stresses and to correlate hemodynamics and geometrical feature with atherosclerotic pathologies [30]. It has been accepted that low and oscillating shear stresses are correlateed positively with intimal thickening and atherosclerosis progression [30, 31]. More recent studies often associated plaque progression and lumen narrowing in carotid bifurcation with elevated high WSS [32, 33]. The most important stresses on the artery wall are the endothelial shear stress due to the blood circulation and the shear stresses due to the expansion of the artery. In addition to fluid shear stress, cyclic strain affects endothelial and vascular smooth muscle cells [34, 35]. For this reason, while many studies were oriented to the carotid hemodynamics in order to establish a direct correlation between blood flow-induced WSS and atherosclerosis localisation [8, 36-39], some others analysed mechanical stresses induced by blood pressure using simplified or patient-specific carotid models [40, 41]. Carotid hemodynamics is very sensitive to geometrical factors as tortuosity, curvature ratio and bifurcations angle [42, 43]. Due to the interindividual variability of

geometry and flow dynamics, this sensitivity is crucial and challenging for computational fluid dynamics (CFD) models and fluid structure interaction (FSI) features. Coupling medical images with computing simulations enables the study of blood flow in human arteries. This has been performed through CFD simulation and, more recently, through FSI analysis with the aim to evaluate the influence of vessel properties on arterial pathologies.

5.2. Geometry meshing

For an image-based analysis four steps are required in order to obtain a WSS map from a 3D image: (a) segmentation, to extract the arterial surface from medical images, (b) volume meshing, to discretize the flow domain, (c) CFD computation and (d) post-processing [44]. Segmentation and patient-specific meshing represent additional complications for the image-based CFD compared to CFD performed on an idealized geometry. In present study, the 3-D geometry has been constructed using a developed automatic vessel lumen segmentation method and results in the geometry as a triangulated surface model (STL) which describes the boundary of a flow domain. Because the partial differential equations (PDE) that govern the fluid flow and arterial wall mechanics do not offers in general an analytical solution, the image-based computational domain (3-D geometry) is split into subdomains, called mesh elements or cells, in which the governing equations are discretized and solved. Different primitives, such as hexahedrons, tetrahedrons and prisms, may be used for the volume discretization (mesh generation) but the type, the

size, the shape quality, the topological arrangement and the orientation of the elements should be chosen with care because they influence the accuracy of the numerical solution.

A series of structured hexahedral meshes and a series of unstructured hybrid meshes of tetrahedrons and prisms are tested for the calculation of the WSS using a CFD analysis [45]. When considering the same artery geometry and the same boundary conditions, a structured hexahedral mesh is found to require a lower number of elements to obtain a mesh-insensitive WSS, enabling more accurate, faster and less memory-demanding computations [refs].

A structured hexahedral meshing protocol for CAB is introduced in present study. The details of the meshing method are presented in the following section.

5.2.1. Hexahedral blocking mesh on ideal carotid artery bifurcation (CAB) geometry

The hexahedral mesh uses a top-down block meshing method and processes in ICEM-CFD (ANSYS Inc. USA) commercial meshing software. The basic concept of this meshing method is to construct virtual blocks whose shape are similar to the vessel geometry, then associating the block edges with the surface curves of the geometry. This top-down meshing method provides a variety of flexible properties to mesh any kinds of shape. The setup of meshing parameters on the virtual blocks is projected to the vessel geometry, and all of this transfer is based on the association protocol which was processed in previous step. The software automatically meshes the geometry based on these parameter settings. The details of block build-up procedure have been shown in Figure 5.1.
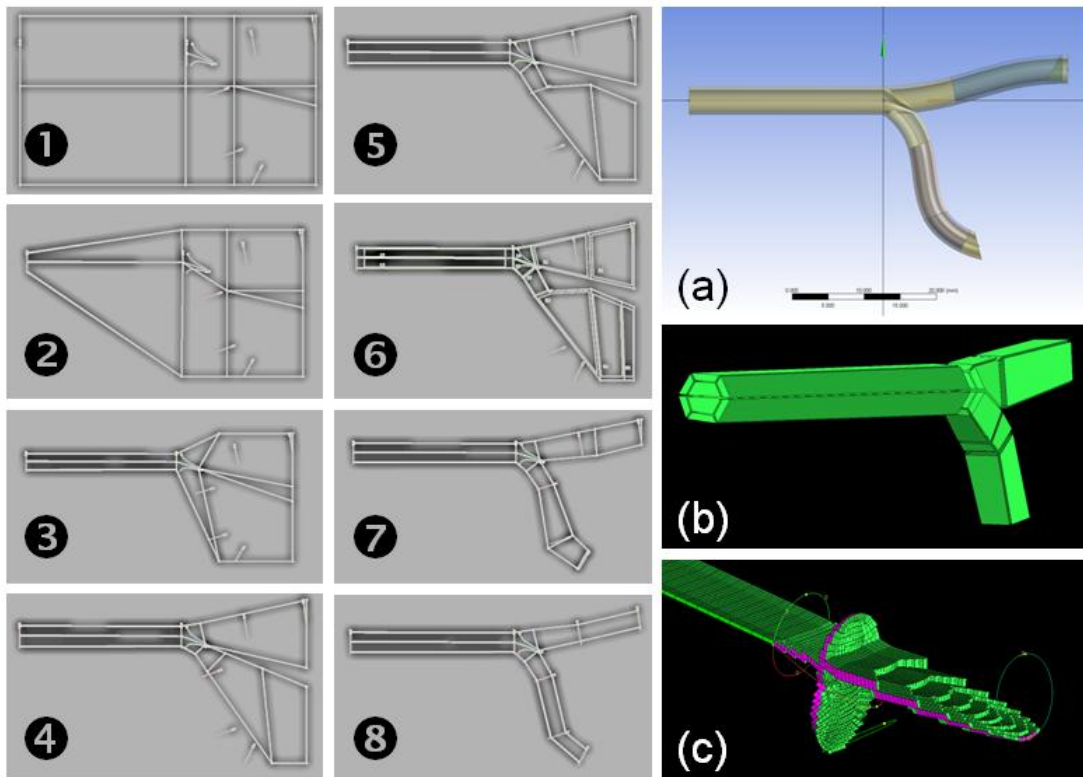
Figure 5.1. The block build-up procedure on ideal vessel bifurcation geometry. This ideal CAB was constructed in CAD program. Figure (1) to Figure (8) shows the block build-up procedure. Figure (a) shows the constructed ideal CAB geometry and Figure (b) shows the appropriate shape of blocks which fit to the geometry. Figure (c) shows the inner hexahedral mesh of bifurcation area.

As Figure 5.1 shows, this process conceptually starts with a single hexahedron block which covers the whole geometry, then slicing and moving the vertex of the edge to an appropriate position, and removing the unnecessary sub-blocks. The geometry-fitted block was constructed as shown in Figure 5.1. (b). Then there needs to set up meshing parameters to command the software to automatically generate the desired mesh. The mesh diagnostics were applied after pre-meshing work. As the fine mesh shown in Figure 5.1 (c), the block meshing method provides hexahedral mesh elements on CAB geometry.

The top-down blocking mesh method for generating hexahedral mesh elements in ideal CAB provides high quality hexahedral mesh elements. The mesh diagnostics also provide a dynamic editing function to mesh quality checking and quality improvement.

5.2.2. Hexahedral blocking mesh on image based CAB geometry

The blocking mesh method is also processed in ultrasound image-based CAB geometry. The procedure of blocking meshing and the result are presented in Figure 5.2. As the results shown in Figure 5.2, the mesh near the bifurcation area has a warped shape but couldn't describe the area well. This is because of the less of the association protocol between block edges and surface of the geometry around the bifurcation area. In previous section, the ideal CAB geometry case has more association protocol on bifurcation area, so that it could provide fine quality hexahedral mesh. The image-based geometry (STL file) generally does not include curve information on surface. The surface curves are needed to generate.
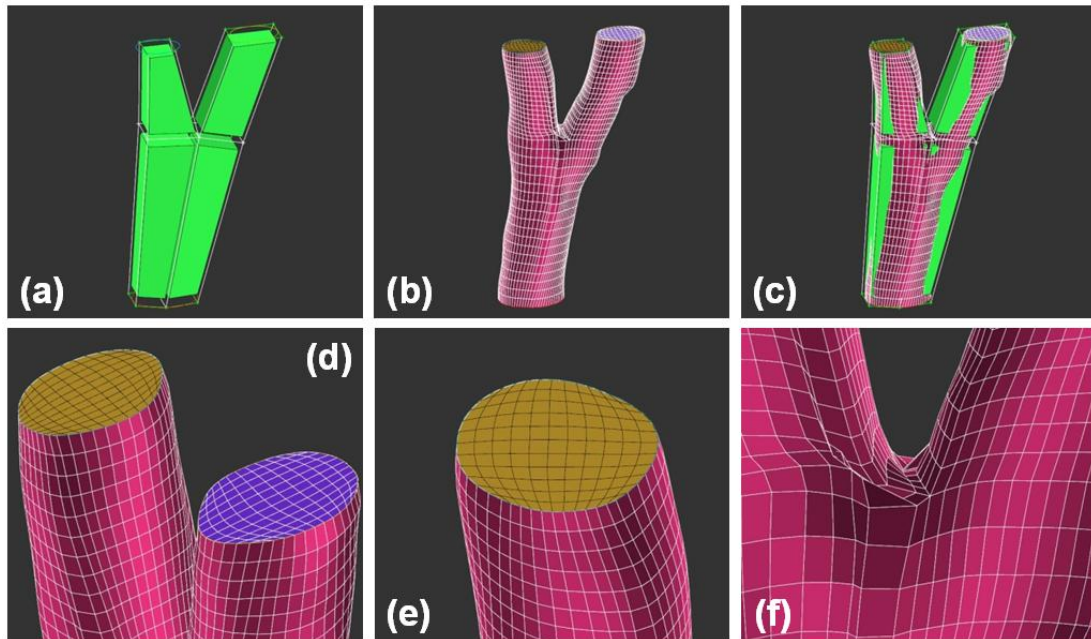
Figure 5.2. The blocking mesh on image based CAB geometry. (a) shows constructed blocks for geometry and (b) shows the generated mesh. (c) shows the combination of (a) and (b) to the association features. (d) and (e) present the zoom-in views of the mesh on ECA and ICA boundary, and ECA, respectively. (f) shows the zoom-in view of the generated mesh on the area of bifurcation apex

The generation of the surface curve on image-based CAB geometry is introduced in Figure 5.3. The first step is to generate eight standard points on the surface of the geometry. Five of them have pointed in bifurcation area as shown in Figure 5.3. (a). The standard curves are generated by connecting these standard points (Figure 5.3. (b)). The surface curves are generated by projecting these six standard curves to the surface of geometry (Figure 5.3. (c)). The projected surface curve and standard curve are displayed together in Figure 5.3. (d).

The surface curves projected in bifurcation area could be used as an association object for blocking meshing. The more detailed association protocol between geometry and virtual block could provide the better meshing result. The hexahedral mesh result on image-based geometry ts presented in Figure 5.4. (c) with o-grid blocking (in Figure 5.4. (b)). The result showing the hexahedral mesh on the bifurcation area is improved and the warped mesh is removed.

The o-grid creation capability is simply the modification of a single block or blocks to a 5 sub-block topology (7 sub-blocks in 3D). The o-grid arranges grid lines into an "O" shape to reduce skew where a block corner lies on a continuous curve or surface. The hexahedral meshing using o-grid could provide better property mesh on the corner or on continuing surface. The meshing result without o-grid block is shown in Figure 5.2. (e), and the skew hexahedral mesh was shown in cross-sectional boundary of ECA on vessel geometry. The improved meshing result using o-grid is shown in Figure 5.5.
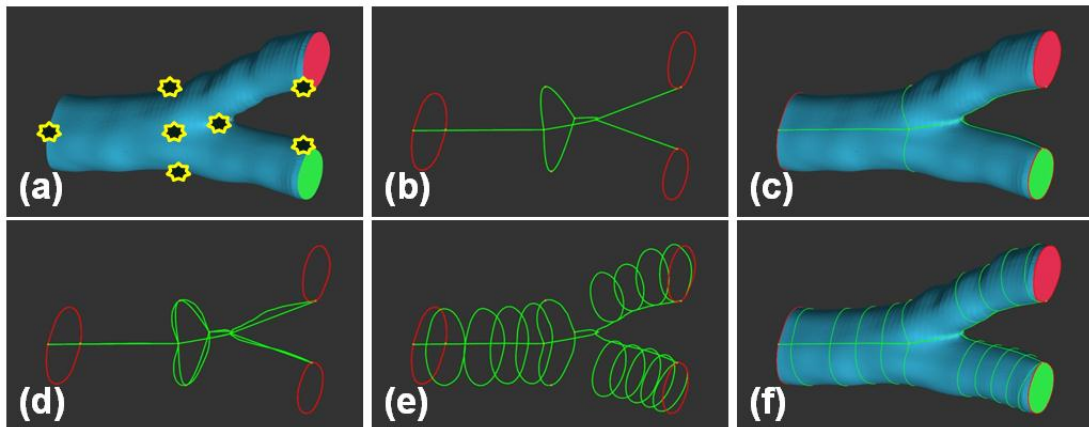
Figure 5.3. The procedure of surface curve generation. Figure (a) shows the standard points and Figure (b) shows the standard curve generated by connecting the standard points. The projected surface curves are shown in Figure (c) and Figure (d). Additional surface curve generation has shown in Figure (e) and Figure (f).
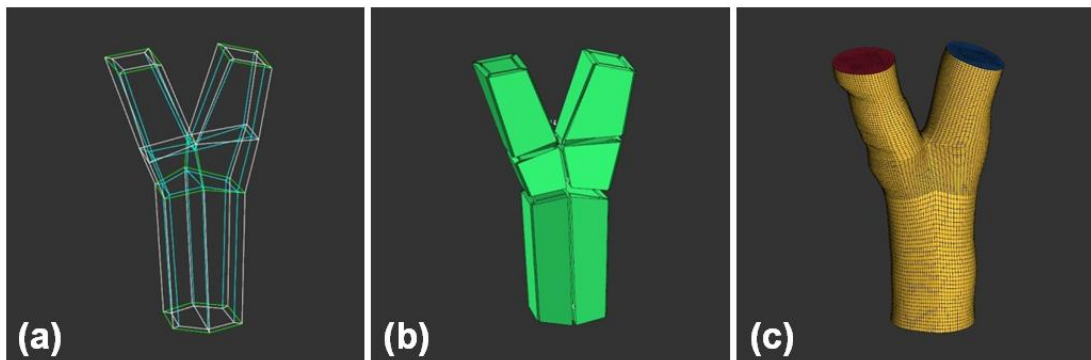
Figure 5.4. The geometry fitted block and the hexahedral meshing result. Figure (a) shows the edges of the block and Figure (b) presents the geometry fitted blocks with o-grid block. The generated hexahedral mesh is shown in (c).
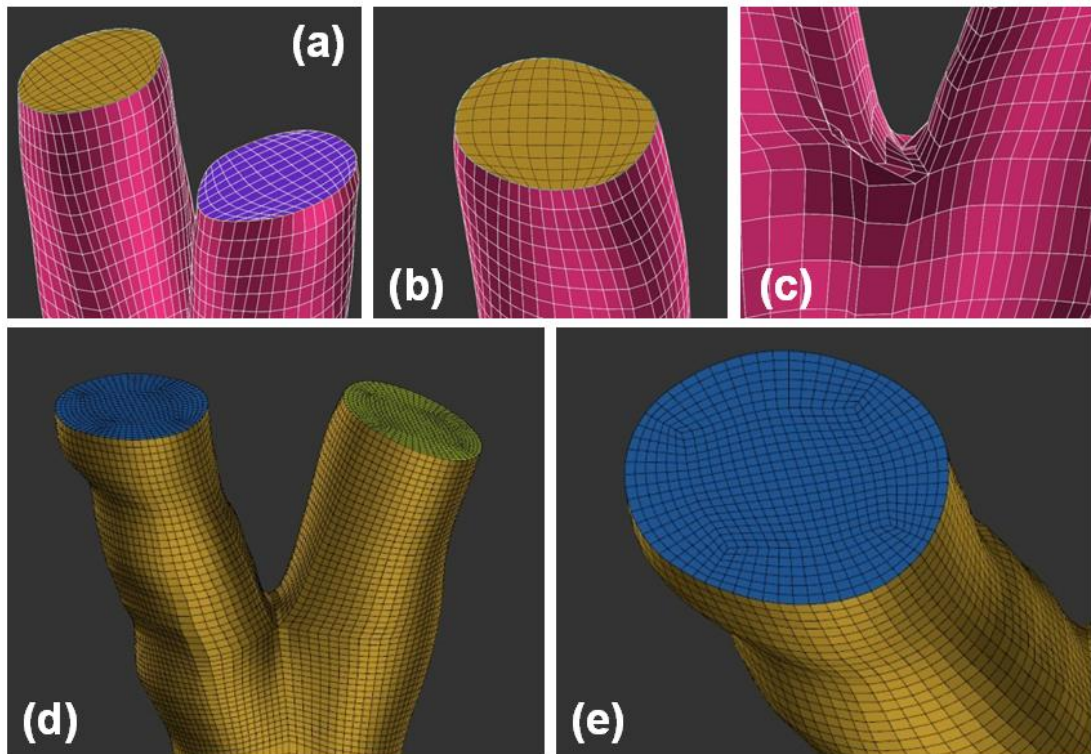
Figure 5.5. The hexahedral mesh comparison between conventional blocking method and o-grid blocking method. (a) and (b) show the meshing results without o-grid blocking, on the contrary the (d) and (e) show the hexahedral meshing with o-grid blocking method. (c) show the contorted mesh on the area of bifurcation apex.

The hexahedral mesh of fluid (lumen geometry) is generated using an o-grid blocking mesh method. The CFD simulation which considers the vessel wall as a rigid wall and using hexahedral mesh as fluid model to calculate the hemodynamics could provide the spatial distribution of WSS on CAB.

It is an on-going work to CFD simulation and not included in this preliminary study. In the present study we have focused on 3-D geometry reconstruction based on medical images. The following simulation work will be covered in future work to evaluate the WSS distribution. The correlation between WSS distribution and plaque generation-progression in a diseased model will also be covered in future study.

Chapter 6

DISCUSSION

Since the carotid artery is one of the important anatomical regions related with cardiovascular diseases such as stenosis and stroke, many studies on US imaging have been focused on characterizing arterial wall mechanics and local hemodynamics in the carotid artery, not only in the clinical practice but also in the basic studies such as the development of segmentation algorithms. In the present study, we investigated the pulsatile variation of 3-D carotid arterial geometry using a novel automatic boundary segmentation approach including the automatic guide point tracking and the scanline edge detection techniques.

The segmentation method of the vessel lumen in longitudinal US image is well developed. An automatic measurement of diameter, dimension and intima media thickness of the aorta have introduce by Tobias Nilsson et al. [46]. But, the longitudinal ultrasound could not provide 3-D geometrical information of the real anatomy and also dependent on the incident angle of acoustic wave. Spyretta Golemati et al. introduced an algorithm using Hough transform to segment longitudinal and transverse sections of the carotid artery [27]. Ying et al. also applied Hough transform for segmentation on cross-sectional US image of carotid artery [28]. Even these works could achieve lumen segmentation in single slice image, but couldn't apply into lumen segmentation of vessel which located in bifurcation zone. To overcome the limitation of current segmentation approach we introduce a novel

detection and segmentation method which using correlation coefficient mapping method (CCM).

The CCM on two consecutive frame images provided several advantages in lumen boundary detection. The first advantage of the CCM method is that provides stable location information about the vessel lumen in US image. Since the large quantity of low correlation area is always occurred in the lumen area, we could use the location information as a guide for automatic tacking of the lumen location. Secondly, using the CCM method, we could significantly reduce the effect of acoustic imaging artifacts on the boundary detection. The echo values in the vessel wall and the surrounding tissues have relatively low variance, and the CC in lumen area is much higher than the one in the other areas. Using this mechanism the influence of shadow artifact by was minimized and low contrast boundary was enhanced.

The CCM method seems to provide vessel-boundary-like edge, but the lumen boundary in CCM is observed to be smaller than that in gray-scale image. This may be due to the lower CC value near the vessel boundary, because the red blood cells have low velocity near the vessel boundary. Furthermore, the lumen boundary in CCM image is getting smaller at the downstream of the bifurcation apex. In this respect, it appears that the boundary information from CCM image is not appropriate to precisely detect the real vessel lumen boundary. During the guide point tracking procedure, inaccurate guide points are appeared on some frames. The CCM image on these frames could not provide a closed boundary at the lumen area. This is probably because the wall motion at these time points has been rapidly

accelerated causing low correlation in full ROI window. We manually set the guide points on this case to segment vessel lumen. In the scanline edge detection method, the automatic segmentation presents increasing error at downstream because the number of un-closed boundary of CCM is increased in this area. Manual fitting is implemented to correct the error points during 3-D geometry construction procedure.

The radially scanning method (scanline) to detect the lumen edge in present study is referred part of star algorithm [47]. In the star algorithm, the standard point (guide point) was manually pointed and the lumen was segmented by radially scanning. The ellipse fitting after edge segmentation seems provide reliable vessel lumen, but in 3-D construction the spatial rotation of long axis of ellipse could results twisted lumen surface after 3-D rendering. The poly nominal fitting on detected lumen edge introduced in present study provide more realistic lumen boundary. The segmented result using scanline method in bifurcation area provides reasonable result which shown in Figure 4.1. Even though the result of polynomial fitted edge is bounding the vessel lumen approximately, there are exceptions that the fitted edge couldn't segment the lumen appropriately. The distort boundary was detected by scanline detection when some of the detected edge is located far away from the guide point or too close to it. A filtering on detected edges is needed to avoid the distort boundary fitting. In present study the sectional fitting procedure is not included. It will be covered in the future study.

Finally, the three-dimensional carotid artery during a cardiac cycle has been constructed

using this automatic boundary segmentation approach. The lumen geometry based on automatic boundary segmentation could be used in CFD analysis for understanding local hemodynamics and hemorheology in the carotid artery. The geometrical cyclic motion of the vessel lumen investigated in present study could provide important information to the FSI simulation results; and also the motion information of 3-D geometry during cardiac cycle could provide boundary conditions for the simulation considering the wall elasticity.

Chapter 7

CONCLUSIONS AND FUTURE WORKS

6.1. Conclusions

A set of 3-D CAB data have acquired in one cardiac cycle using high frame rate ultrasound imaging mode (EKV) which commercially available in Vevo 770 system. The data set was acquired using an ultrasound probe with 40 MHz center frequency on rat model. The acquired cross-sectional image represents the cyclic variation of vessel lumen with 1000 frames per a minute, in other words 200 frames per a cardiac cycle.

This is the first work that combined CCM guide point tracking and scanline edge detection algorithm for automatically segment the vessel lumen. The guide point tracking method using CCM approach provides a robust center-point tracking characteristic. The segmentation in bifurcation area where combines two vessel lumens is also provide stable tracking results. The vessel lumen segmentation in low contrast US image with shadow artifacts could achieve using scanline edge detection algorithm based on tracked CCM guide points.

The fluid shear is generated by friction or viscous drag due to blood flow acts tangentially (WSS) upon the vascular wall and endothelium. The magnitude of fluid shear depends on factors such as local geometry of the vessel, local velocity of blood flow and the viscosity of blood as largely related to the hematocrits. The distribution of WSS by

numerical simulation is influenced by local geometry. For the first time the temporal variation of 3-D carotid artery geometry have constructed in this study. The temporal variation of 3-D CAB geometry could provide referential information for checking the results of numerical simulation.

Vessel wall motion, caused by blood pressure, blood flow and tethering to the surrounding tissue may be responsible for tissue rupture and cerebrovascular symptoms. The motion of vessel wall provides important information to clinical diagnosis. In present study, asymmetric wall motion during a vascular cyclic has investigated in both CCM image based and automatic segmentation based 3-D geometry. This asymmetric mechanism leads us to design more realistic boundary conditions for numerical simulation and help us to know the pathology of artery stenosis in CAB.

6.2. Future works

The 3-D geometry construction on patient specific image data need to be included in the future study. The comparison between diseased model and normal model could lead us to know the relation between pathology of the vascular disease and vessel motion. A 3-D geometry construction system on real time could be imported in clinic for diagnosis.

An upgrade of automatic guide point tracking method and scanline edge detection method are needed for reducing the segmentation error and the calculating time. A segmentation approach which considered the CAB with plaque is also need to consider in

future research.

The CFD simulation will be carried in, for evaluate the distribution of WSS that based on constructed 3-D geometry. The numerical simulation (FSI) which considered vessel wall elasticity could provide more realistic result by referring the information of 3-D vessel motion. These simulations help us to know the hemodynamics in CAB more clearly.

Currently, the 3-D geometry construction is progressed in commercial software; the operation software switching work is tedious and time consuming. An all-process-combined work flow in single software should be developed and more robust edge detection approach needs to be carried in the future work. In addition, the CCM image boundary carries useful clinical information about rheology of blood flow. In our knowledge there is no research have been discovered on this mechanism. Hence the quantitate analysis of the CCM image based geometry should be studied.

BIBLIOGRAPHY

[1]   A. Towfighi and J. L. Saver, "Stroke declines from third to fourth leading cause of death in the United States: historical perspective and challenges ahead," *Stroke,* vol. 42, pp. 2351-5, Aug 2011.

[2]   K. H. Nam, T. H. Bok, C. Jin, and D. G. Paeng, "Asymmetric radial expansion and contraction of rat carotid artery observed using a high-resolution ultrasound imaging system," *Ultrasonics,* vol. 54, pp. 233-40, Jan 2014.

[3]   J. C. Fruchart, M. C. Nierman, E. S. Stroes, J. J. Kastelein, and P. Duriez, "New risk factors for atherosclerosis and patient risk assessment," *Circulation,* vol. 109, pp. III15-9, Jun 15 2004.

[4]   C. Wang, M. Chen, S. L. Liu, Y. Liu, J. M. Jin, and Y. H. Zhang, "Spatial distribution of wall shear stress in common carotid artery by color Doppler flow imaging," *J Digit Imaging,* vol. 26, pp. 466-71, Jun 2013.

[5]   H. J. Mutsaerts, I. H. Palm-Meinders, A. J. de Craen, J. H. Reiber, G. J. Blauw, M. A. van Buchem*, et al.*, "Diastolic carotid artery wall shear stress is associated with cerebral infarcts and periventricular white matter lesions," *Stroke,* vol. 42, pp. 3497-501, Dec 2011.

[6]   G. S. van Bochove, R. Straathof, R. Krams, K. Nicolay, and G. J. Strijkers, "MRI-determined carotid artery flow velocities and wall shear stress in a mouse model of vulnerable and stable atherosclerotic plaque," *MAGMA,* vol. 23, pp. 77-84, Apr 2010.

[7]   M. Markl, F. Wegent, T. Zech, S. Bauer, C. Strecker, M. Schumacher*, et al.*, "In vivo wall shear stress distribution in the carotid artery: effect of bifurcation geometry, internal carotid artery stenosis, and recanalization therapy," *Circ Cardiovasc Imaging,* vol. 3, pp. 647-55, Nov 2010.

[8]   D. Gallo, D. A. Steinman, P. B. Bijari, and U. Morbiducci, "Helical flow in carotid bifurcation as surrogate marker of exposure to disturbed shear," *J Biomech,* vol. 45, pp. 2398-404, Sep 21 2012.

[9]   E. Chytilova and J. Malik, "[Wall shear stress in carotid artery and its role in the development of atherosclerosis]," *Vnitr Lek,* vol. 53, pp. 377-81, Apr 2007.

[10]   Y. Jiang, K. Kohara, and K. Hiwada, "Low wall shear stress contributes to atherosclerosis of the carotid artery in hypertensive patients," *Hypertens Res,* vol. 22, pp. 203-7, Sep 1999.

[11]   A. V. Kamenskiy, J. N. MacTaggart, Pipinos, II, J. Bikhchandani, and Y. A. Dzenis, "Three-dimensional geometry of the human carotid artery," *J Biomech Eng,* vol. 134, p. 064502, Jun 2012.

[12]   H. Y. Sun, Y. Li, K. Guo, X. N. Kang, C. Sun, and Y. K. Liu, "[Identification of

metastasis-related osteopontin expression and glycosylation in hepatocellular carcinoma]," *Zhonghua Gan Zang Bing Za Zhi,* vol. 19, pp. 904-7, Dec 2011.

[13] Y. Li, H. Jia, Q. Yan, Z. Jiang, and S. Yang, "[Improvement of catalytic capability of Paecilomyces thermophila J18 thermostable beta-1,3-1,4-glucanase under acidic condition by directed evolution]," *Sheng Wu Gong Cheng Xue Bao,* vol. 27, pp. 1797-804, Dec 2011.

[14] S. Wei and Y. Li, "[Functions of plant phosphoenolpyruvate carboxylase and its applications for genetic engineering]," *Sheng Wu Gong Cheng Xue Bao,* vol. 27, pp. 1702-10, Dec 2011.

[15] A. M. Malek and S. Izumo, "Control of endothelial cell gene expression by flow," *J Biomech,* vol. 28, pp. 1515-28, Dec 1995.

[16] D. Feller-Kopman, "Ultrasound-guided thoracentesis," *Chest,* vol. 129, pp. 1709-14, Jun 2006.

[17] E. Cherin, R. Williams, A. Needles, G. Liu, C. White, A. S. Brown*, et al.*, "Ultrahigh frame rate retrospective ultrasound microimaging and blood flow visualization in mice in vivo," *Ultrasound Med Biol,* vol. 32, pp. 683-91, May 2006.

[18] U. Schminke, L. Motsch, L. Hilker, and C. Kessler, "Three-dimensional ultrasound observation of carotid artery plaque ulceration," *Stroke,* vol. 31, pp. 1651-5, Jul 2000.

[19] D. C. Barratt, B. B. Ariff, K. N. Humphries, S. A. Thom, and A. D. Hughes, "Reconstruction and quantification of the carotid artery bifurcation from 3-D ultrasound images," *IEEE Trans Med Imaging,* vol. 23, pp. 567-83, May 2004.

[20] J. Yao, M. R. van Sambeek, A. Dall'Agata, L. C. van Dijk, M. Kozakova, P. J. Koudstaal*, et al.*, "Three-dimensional ultrasound study of carotid arteries before and after endarterectomy; analysis of stenotic lesions and surgical impact on the vessel," *Stroke,* vol. 29, pp. 2026-31, Oct 1998.

[21] C. Palombo, M. Kozakova, C. Morizzo, F. Andreuccetti, A. Tondini, P. Palchetti*, et al.*, "Ultrafast three-dimensional ultrasound: application to carotid artery imaging," *Stroke,* vol. 29, pp. 1631-7, Aug 1998.

[22] J. C. Seabra, L. M. Pedro, J. F. e Fernandes, and J. M. Sanches, "A 3-D ultrasound-based framework to characterize the echo morphology of carotid plaques," *IEEE Trans Biomed Eng,* vol. 56, pp. 1442-53, May 2009.

[23] M. Dong, M. G. Eramian, S. A. Ludwig, and R. A. Pierson, "Automatic detection and segmentation of bovine corpora lutea in ultrasonographic ovarian images using genetic programming and rotation invariant local binary patterns," *Med Biol Eng Comput,* vol. 51, pp. 405-16, Apr 2013.

[24] A. Fenster, C. Blake, I. Gyacskov, A. Landry, and J. D. Spence, "3D ultrasound analysis of carotid plaque volume and surface morphology," *Ultrasonics,* vol. 44 Suppl 1, pp. e153-7, Dec 22 2006.

[25]   A. Krasinski, B. Chiu, J. D. Spence, A. Fenster, and G. Parraga, "Three-dimensional ultrasound quantification of intensive statin treatment of carotid atherosclerosis," *Ultrasound Med Biol,* vol. 35, pp. 1763-72, Nov 2009.

[26]   M. Egger, J. D. Spence, A. Fenster, and G. Parraga, "Validation of 3D ultrasound vessel wall volume: an imaging phenotype of carotid atherosclerosis," *Ultrasound Med Biol,* vol. 33, pp. 905-14, Jun 2007.

[27]   S. Golemati, J. Stoitsis, E. G. Sifakis, T. Balkizas, and K. S. Nikita, "Using the Hough transform to segment ultrasound images of longitudinal and transverse sections of the carotid artery," *Ultrasound Med Biol,* vol. 33, pp. 1918-32, Dec 2007.

[28]   Y. Li, T. H. Bok, J. H. Yang, M. J. Choi, and D. G. Paeng, "The acute effects of smoking on the cyclic variations in blood echogenicity of carotid artery," *Ultrasound Med Biol,* vol. 37, pp. 513-21, Apr 2011.

[29]   J. Renner, H. Nadali Najafabadi, D. Modin, T. Lanne, and M. Karlsson, "Subject-specific aortic wall shear stress estimations using semi-automatic segmentation," *Clin Physiol Funct Imaging,* vol. 32, pp. 481-91, Nov 2012.

[30]   D. N. Ku, D. P. Giddens, C. K. Zarins, and S. Glagov, "Pulsatile flow and atherosclerosis in the human carotid bifurcation. Positive correlation between plaque location and low oscillating shear stress," *Arteriosclerosis,* vol. 5, pp. 293-302, May-Jun 1985.

[31]   D. P. Giddens, C. K. Zarins, and S. Glagov, "The role of fluid mechanics in the localization and detection of atherosclerosis," *J Biomech Eng,* vol. 115, pp. 588-94, Nov 1993.

[32]   D. Tang, C. Yang, S. Kobayashi, and D. N. Ku, "Steady flow and wall compression in stenotic arteries: a three-dimensional thick-wall model with fluid-wall interactions," *J Biomech Eng,* vol. 123, pp. 548-57, Dec 2001.

[33]   D. Tang, C. Yang, J. Zheng, P. K. Woodard, G. A. Sicard, J. E. Saffitz*, et al.*, "3D MRI-based multicomponent FSI models for atherosclerotic plaques," *Ann Biomed Eng,* vol. 32, pp. 947-60, Jul 2004.

[34]   H. F. Younis, M. R. Kaazempur-Mofrad, R. C. Chan, A. G. Isasi, D. P. Hinton, A. H. Chau*, et al.*, "Hemodynamics and wall mechanics in human carotid bifurcation and its consequences for atherogenesis: investigation of inter-individual variation," *Biomech Model Mechanobiol,* vol. 3, pp. 17-32, Sep 2004.

[35]   H. F. Younis, M. R. Kaazempur-Mofrad, C. Chung, R. C. Chan, and R. D. Kamm, "Computational analysis of the effects of exercise on hemodynamics in the carotid bifurcation," *Ann Biomed Eng,* vol. 31, pp. 995-1006, Sep 2003.

[36]   K. Perktold, R. O. Peter, M. Resch, and G. Langs, "Pulsatile non-Newtonian blood flow in three-dimensional carotid bifurcation models: a numerical study of flow phenomena under different bifurcation angles," *J Biomed Eng,* vol. 13,

pp. 507-15, Nov 1991.

[37]   J. A. Moore, B. K. Rutt, S. J. Karlik, K. Yin, and C. R. Ethier, "Computational blood flow modeling based on in vivo measurements," *Ann Biomed Eng,* vol. 27, pp. 627-40, Sep-Oct 1999.

[38]   J. A. Moore, D. A. Steinman, D. W. Holdsworth, and C. R. Ethier, "Accuracy of computational hemodynamics in complex arterial geometries reconstructed from magnetic resonance imaging," *Ann Biomed Eng,* vol. 27, pp. 32-41, Jan-Feb 1999.

[39]   U. Morbiducci, D. Gallo, R. Ponzini, D. Massai, L. Antiga, F. M. Montevecchi*, et al.*, "Quantitative analysis of bulk flow in image-based hemodynamic models of the carotid bifurcation: the influence of outflow conditions as test case," *Ann Biomed Eng,* vol. 38, pp. 3688-705, Dec 2010.

[40]   D. A. Steinman, D. A. Vorp, and C. R. Ethier, "Computational modeling of arterial biomechanics: insights into pathogenesis and treatment of vascular disease," *J Vasc Surg,* vol. 37, pp. 1118-28, May 2003.

[41]   I. Hariton, G. deBotton, T. C. Gasser, and G. A. Holzapfel, "Stress-modulated collagen fiber remodeling in a human carotid bifurcation," *J Theor Biol,* vol. 248, pp. 460-70, Oct 7 2007.

[42]   J. B. Thomas, J. S. Milner, and D. A. Steinman, "On the influence of vessel planarity on local hemodynamics at the human carotid bifurcation," *Biorheology,* vol. 39, pp. 443-8, 2002.

[43]   S. W. Lee, L. Antiga, J. D. Spence, and D. A. Steinman, "Geometry of the carotid bifurcation predicts its exposure to disturbed flow," *Stroke,* vol. 39, pp. 2341-7, Aug 2008.

[44]   D. A. Steinman, "Image-based computational fluid dynamics modeling in realistic arterial geometries," *Ann Biomed Eng,* vol. 30, pp. 483-97, Apr 2002.

[45]   G. De Santis, M. De Beule, K. Van Canneyt, P. Segers, P. Verdonck, and B. Verhegghe, "Full-hexahedral structured meshing for image-based computational vascular modeling," *Med Eng Phys,* vol. 33, pp. 1318-25, Dec 2011.

[46]   T. Nilsson, S. Segstedt, P. Milton, S. Sveinsdottir, T. Jansson, H. W. Persson*, et al.*, "Automatic Measurements of Diameter, Distension and Intima Media Thickness of the Aorta in Premature Rabbit Pups Using B-Mode Images," *Ultrasound Med Biol,* Nov 20 2013.

[47]   J. Guerrero, S. E. Salcudean, J. A. McEwen, B. A. Masri, and S. Nicolaou, "System for deep venous thrombosis detection using objective compression measures," *IEEE Trans Biomed Eng,* vol. 53, pp. 845-54, May 2006.

ACKNOWLEGEMENTS

아름다운 제주에서 학문을 터득하고 지식을 쌓아가게 된 것은 너무 감사한 일입니다. 팽동국 교수님을 저의 대학원 지도교수로 모시게 된 것은 큰 행운입니다. 본질적인 문제에 대한 교수님의 아낌없는 조언과 진실한 말씀들이 부족한 저에게는 너무나 마땅한 교훈과 도움이 되었습니다. 교수님을 만나게끔 이끌어 주심에 늘 감사하며 다시 한번 고개 숙여 존경하는 마음을 전합니다. 그리고 가르침과 조언을 아끼지 않으시는 이종현 교수님, 영상처리의 새로운 필드로 이끌어 주신 배진호 교수님께 감사 드립니다. 그리고 조일형 교수님께 감사를 드립니다. 교수님들의 관심과 격려를 잊지 않고 있습니다. 그리고 지금은 제주에 계시지 않지만 열정으로 가르쳐 주셨던 유원선 교수님 감사 드립니다.

열정으로 연구하시고 차분하시며 친절한 남권호 박사님께 감사 드립니다. 부족한 저의 논문을 일일이 수정해 주시고 많은 자료와 아이디어들을 아낌없이 공유해 주신 큰 덕에 저 또한 많은 것을 배우게 되었습니다. 지금은 멀리 있지만 대학원에 금방 들어왔을 때 많은 도움을 주셨고 솔직한 이야기를 나눌 수 있었던 복태훈 박사님께 감사 드립니다. 컴퓨터 시뮬레이션에 대한 많은 지식과 상식들을 공유하신 고혁준 박사님 감사 드립니다. 영상처리에 실질적인 도움을 아끼지 않았던 포항공대 염은섭 선배님, 의공학 협동과정의 능력자 관석이형에게도 감사 드립니다. 그리고 우리 연구실의 주축이신 '만능해결사' 주호형에게 감사 드립니다. 형의 묵묵히 무거운 짐을 지고 잘 감당해 나가는 모습이 저희에게는 늘 도전이 됩니다. 친 누나와 같고 따뜻한 마음의 소유자 윤정 누나, 늘 자신감이 넘치고 최선을 다하는 바다의 남자 정록이형, 아내로써 또한 연구자로써 필드에서 열심히 뛰고 있는 孔琦, 그리고 그의 남편 刘萧에게 감사 드립니다. 그리고 유쾌한 시간을 만들어 주었던 대희형, 키다리 아저씨 종헌형, 영리한 '너구리' 혜빈이, 그리고 '차박사' 한수, 연구를 차근차근 해 나가는 종우에게 감사를 드립니다. 동기이자 후배인

'왜'의 달인 기철이 고맙다. 너도 곧 논문을 쓸 텐데 만족하는 결과 있기를 바란다. 그리고 학사 행정관리에 많은 도움을 주셨던 김은영 조교선생님 감사합니다. 많이 도와주신 덕분에 무사히 졸업할 수 있었던 것 같습니다.

학문의 '진미'를 맛보게 한 연변과학기술대학교 문용찬교수님, 꿈의 씨앗을 심어주신 문규성 교수님, 늘 친절한 친구처럼 대화를 이끌어 주신 Martin Groß 에게 감사 드립니다. 그리고 제주에 머무는 동안 저에게 영적으로 많은 힘이 되셨던 조현직 교수님께 감사 드립니다. 대학원에 지원하는 일부터 지금까지 여러모로 많은 도움을 주신 박미선 선배 에게도 감사 드립니다. 과기대 교수님들과 선배들을 통하여 받은 사랑의 빚을 평생토록 갚겠습니다.

마지막으로 이 논문이 완성될 때까지 묵묵히 응원해 주신 가족께 감사 드립니다. 저를 낳으시고 성장시켜준 아버지, 부지런히 뒷받임을 해 주신 어머니께 감사의 마음을 전합니다. 아껴 쓰면서 저의 학부과정 등록금을 전부 지원해 준 늘 고마운 우리 누나, 이젠 누나도 엄마가 되여서 행복하게 사랑을 나누며 살기를 축복해요.

모두 건강하시고 하는 일이 형통하기를 기원하면서 감사의 글을 줄입니다.

2014 년 02 월

김창수.

CURRICULUM VITAE

Changzhu Jin

Date of Birth: 21 Mar. 1988
Nationality: The people republic of China
Male / single
Address: Department of Ocean System Engineering, Jeju National
University (Jeju NU), Jeju si, 690-756, Korea
Email: yustchang@jejunu.ac.kr

Education

M.E.	Jeju National University, Jeju, Korea
Mar 2012	Ocean System Engineering
-Feb 2014	Supervisor: Dong-Guk Paeng
B.E	Yangbian University of science and technology, Yanji, China
Sep 2007	Materials, Mechanical & Automation Engineering
-June 2011	Supervisor: Yong-Chan Moon

Research experience

Dec 2012 - Present	Research assistant at Ocean System Engineering,(SBAN project), Jeju NU

- Primary system preparation of SBAN project.
- The 1st SBAN signal transmitting and receiving experiment in DSME.

May 2012 - Nov 2012	Research assistant at Ocean System Engineering, Jeju NU

- The noise level evaluation of construction site near the aqua farm.
- 3-D dataset acquisition of carotid artery bifurcation using high frequency-frame rate ultrasound imaging on rat subjects.
- The cyclic variation of 3-D carotid artery geometry from ultrasound imaging.

Awards

June 2013   Presidential Award for an Outstanding Academic Paper (Jeju NU)
Dec 2013   Excellence paper award, the 14th annual Conference of the
                 Biomedical Engineering Society for circulation (Korea)

Publications

1.   Kweon-Ho Nam, Tae-Hoon Bok, <u>Changzhu Jin</u> and Dong-Guk Paeng, "Asymmetric
      radial expansion and contraction of rat carotid artery observed using a
      high-resolution ultrasound imaging system", Ultrasonics, 54,(2014),233-240

Conference

1.   <u>Changzhu Jin</u>, Kweon-Ho Nam and Dong-Guk Paeng, "Automatic lumen
      segmentation from the cross-sectional ultrasound images of the rat carotid artery
      bifurcation", the 14th Annual Conference of the Biomechanical Engineering Society
      for Circulation.P-13,(2013),in Seoul.
2.   <u>Changzhu Jin</u>, Kweon-Ho Nam, Tae-Hoon Bok and Dong-Guk Paeng, "Cyclic
      variation of three-dimensional geometry of the rat carotid artery bifurcation assessed
      by high-frequency ultrasound imaging". J.Acoust. Soc. Am. 134, 4215, (2013), in
      Sanfransisco.
3.   <u>Changzhu Jin</u>, Kweon-Ho Nam and Dong-Guk Paeng, "3-D geometry of the Rat
      Carotid Artery Bifurcation Based on High-Frequency Ultrasound Imaging and
      Hexahedral Meshing", the 13th Annual Conference of the Biomechanical
      Engineering Society for Circulation.P-33, (2013), in Gwangju.